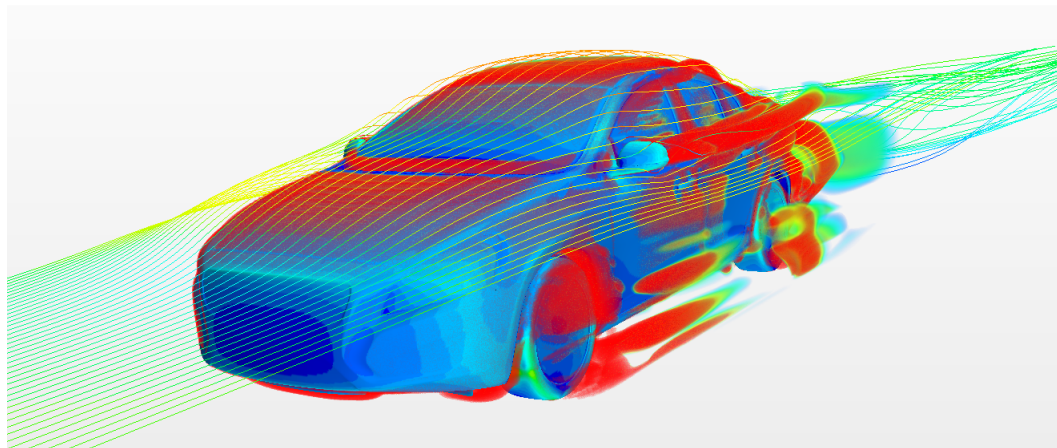


CHALMERS



Flow structure investigation of a Volvo S60

Bachelor's thesis in Applied Mechanics

TIM DEKKER

EFREM EFREMOV

SAM NASSIRI

SIMON STORM

BJÖRN WALLIN

Department of Applied Mechanics

Division of Vehicle Engineering & Autonomous Systems

CHALMERS UNIVERSITY OF TECHNOLOGY

Gothenburg, Sweden 2016

Bachelor's Thesis 2016:06

Bachelor's thesis 2016:06

Flow structure investigation of a Volvo S60

TIM DEKKER
EFREM EFREMOV
SAM NASSIRI
SIMON STORM
BJÖRN WALLIN



CHALMERS
UNIVERSITY OF TECHNOLOGY

Department of Applied Mechanics
Division of Vehicle Engineering & Autonomous Systems
Chalmers University of Technology
Gothenburg, Sweden 2016

TIM DEKKER
EFREM EFREMOV
SAM NASSIRI
SIMON STORM
BJÖRN WALLIN

©TIM DEKKER EFREM EFREMOV SAM NASSIRI SIMON STORM
BJÖRN WALLIN, 2016.

Supervisor: Sabine Bonitz
Examiner: Simone Sebben

Bachelor's thesis 2016:06
ISSN 1654-4676
Department of Applied Mechanics
Division of Vehicle Engineering and Autonomous Systems
Chalmers University of Technology
SE-412 96 Gothenburg
Telephone +46 31 772 1000

Abstract

Reducing aerodynamic drag is a major goal in vehicle design and the positive impact of reduced drag on fuel consumption is well-documented. Drag is influenced by the physical phenomena around a passenger car. It is thus imperative to better understand the flow structures on a passenger car. This study investigates the flow structures occurring on the rear of a Volvo S60, conducted in STAR-CCM+. The flow structures were observed for varying Reynolds number, varying yaw angle and with and without an antenna.

The results show that the pressure coefficient and skin friction coefficient change slightly at different Reynolds numbers. How they change depends on where on the vehicle the coefficients are analyzed. The varying yaw angle impacts the pressure coefficient and the skin friction coefficient by shifting the structures away from the direction of the flow. The antenna case shows that the flow is disrupted by two opposing vortices which impact the pressure coefficient and the skin friction coefficient.

The skin friction coefficient and pressure coefficient changed with the velocity but this did not have any apparent effect on the drag coefficient. For the yaw angle study it was the other way around; all three parameters changed with an increase in yaw which thus meant that the flow structure on the car had a yaw angle dependency. The antenna showed a distinct alteration of the flow structure. An increase of skin friction in line with the antenna was detected from the window to the end of the boot lid. Also an increase in pressure over the bottom of the rear window could be identified. However, the antenna did not affect the drag coefficient in any significant way.

Sammandrag

En viktig del i fordonsutveckling är att minimera luftmotståndet då dess positiva inverkan på bränsleförbrukningen är väldokumenterad. Luftmotstånd påverkas av flödet runt fordonet och därför är det av stor vikt att ha god förståelse för flödesstrukturen runt fordonet. Den här studien undersöker flödesstrukturen runt bakre halvan på en Volvo S60 med hjälp av STAR-CCM+. Flödesstrukturen undersöktes för varierande Reynolds tal, yaw vinklar och med och utan en antenn på bilen.

Resultaten visade att ytfriktionskoefficienten och tryckkoefficienten förändrades vid varierande Reynolds tal. Hur de förändrades berodde på var på bilen koefficienterna undersöktes. En varierande yaw vinkel påverkade koefficienterna genom att förskjuta dess flödesstrukturer bort från flödet. I fallet med och utan antenn, visades det att med antenn blev flödet bakom denne omtumlat med två motarbetande vortexter. Detta påverkade både tryckkoefficienten och ytfriktionskoefficienten.

Trots varierande hastighet och förändringar i ytfriktionskoefficienten och tryckkoefficienten, förblev drag koefficienten oförändrad. Däremot genererade en förändring av yaw vinkeln en förändring av de tre tidigare nämnda parametrarna. Således tyder detta på ett yaw vinkel beroende. Antennstudien visade förändringar av flödesstrukturen och en distinkt ökning av ytfriktionen i linje med antennen. Denna yta sträckte sig från övre kanten på bakrutan till slutet på bakluckan. Dessutom kunde en tydlig tryckökning påvisas vid nedre kanten av bakrutan. Dock hade dessa flödesstrukturändringar låg inverkan på drag koefficienten.

Acknowledgements

We would like to express our sincerest gratitude to Sabine Bonitz for her guidance and expertise as our supervisor. Her steadfast devotion to working with fluid dynamics has been a great motivation and inspiration.

We also wish to thank Simone Sebben for the opportunity to work with this bachelor thesis.

Finally, we would like to thank Magnus Urquhart for his advice and excellent assistance with Star CCM+.

The Authors, Göteborg 17/05/16

Contents

Nomenclature	xi
1 Introduction	1
1.1 Objective	2
1.2 Delimitation	2
2 Theory	3
2.1 Fluid Mechanics	3
2.1.1 Reynolds number	3
2.1.2 Reynolds transport theorem	3
2.1.3 Conservation of mass and momentum	4
2.1.4 Boundary layer theory	5
2.1.5 Separation	6
2.1.6 Surface pressure coefficient	8
2.1.7 Vorticity	9
2.1.8 Q-criterion	9
2.1.9 Skin friction coefficient	10
2.1.10 Aerodynamic forces	10
2.1.11 Yaw angle	11
2.2 Computational Fluid Dynamics	12
2.2.1 The finite volume method	12
2.2.2 Turbulence modelling	13
2.2.3 Compressible and incompressible flow	17
3 Method	18
3.1 Literature Review	18
3.2 CFD and STAR-CCM+	18
3.2.1 Geometry preparation and setting up boundaries	19
3.2.2 Mesh generation	19
3.2.3 Setting up physics and solver settings	21

3.2.4	Setting up the yaw conditions	22
3.2.5	Convergence	23
3.3	Investigated Cases	23
3.4	Post-processing	23
4	Results and Analysis	24
4.1	Validation of Simulations	24
4.2	Valid y^+ Values	26
4.3	Reynolds Dependency	26
4.3.1	Drag coefficient	27
4.3.2	Surface pressure coefficient	28
4.3.3	Skin friction coefficient	30
4.4	Antenna Study	35
4.4.1	Drag coefficient	35
4.4.2	Surface pressure coefficient	35
4.4.3	Skin friction coefficient	38
4.5	Yaw Angle Dependency	41
4.5.1	Drag coefficient	41
4.5.2	Surface pressure coefficient	42
4.5.3	Skin friction coefficient	44
5	Discussion	46
5.1	Reynolds Dependency	46
5.2	Antenna Impact	47
5.3	Yaw Angle	48
6	Conclusion	50
6.1	Reynolds Dependency	50
6.2	Antenna Impact	51
6.3	Yaw Angle	51
6.4	Further Study	52
6.5	Evaluation	52
	Bibliography	56
	APPENDICES	I
A	y^+ Values	I
B	Surface Pressure Coefficient	III
C	Skin friction coefficient	IV

Nomenclature

CAD	Computer Aided Design
CFD	Computational Fluid Dynamics
CS	Control Surface
CV	Control Volume
Drag count	The third significant decimal in the drag coefficient
DriveAer	Car model developed by collaboration between BMW and Audi
FVM	Finite Volume Method
k- ε -model	turbulence model
PDE	Partial Differential Equation
RANS	Reynolds Averaged Navier Stokes
SAE	Society of Automotive Engineers
StarCCM+	CFD software
TDR	Turbulent Dissipation Rate
a	acceleration [$\frac{m}{s^2}$]
a	speed of sound [$\frac{m}{s}$]
B	property of a fluid [-]
β	intensive value of B [$\frac{dB}{dm}$]
c_1	user-defined constant [-]
c_2	user-defined constant [-]
C_D	drag coefficient [-]
C_L	lift coefficient [-]
C_p	pressure coefficient [-]
δ	boundary layer thickness [m]
D	downforce [N]
F	force [N]

F_P	pressure drag[N]
F_F	friction drag[N]
F_D	drag force[N]
F_L	lift force[N]
g	gravitational constant [$\frac{m}{s^2}$]
G_b	Turbulence kinetic energy due to buoyancy [$\frac{J}{kg}$]
G_k	Turbulence kinetic energy due to the mean velocity gradients [$\frac{J}{kg}$]
h	distance of a limiting streamline from the surface[m]
k	turbulent kinetic energy [$\frac{J}{kg}$]
L	length travelled[m]
m	mass[kg]
Ma	Mach[-]
μ	dynamic viscosity of the fluid [$Pa \cdot s$]
∇	gradient[-]
ν	kinematic viscosity [$\frac{kg}{m \cdot s}$]
ω	vorticity vector [$\frac{1}{s}$]
p_∞	static pressure of the incident flow[Pa]
p	local static pressure[Pa]
Re	reynolds number[-]
ρ	density [$\frac{kg}{m^3}$]
ρ_∞	free stream density [$\frac{kg}{m^3}$]
σ_k	turbulent Prandtl number for k[Pa]
σ_ϵ	turbulent Prandtl number for epsilon[Pa]
S_k	user-defined source term [-]
S_ϵ	user-defined source term[-]
t	time[s]

τ_w	wall shear stress[Pa]
u^+	dimensionless velocity near wall[-]
u^*	friction velocity[$\frac{m}{s}$]
u_∞	free stream velocity[$\frac{m}{s}$]
u'	fluctuating part of velocity[$\frac{m}{s}$]
\bar{u}	time-averaged velocity[$\frac{m}{s}$]
u	local velocity[$\frac{m}{s}$]
u, v, w	velocity components[$\frac{m}{s}$]
V	velocity[$\frac{m}{s}$]
V_r	relative velocity[$\frac{m}{s}$]
\mathbf{v}	velocity vector[$\frac{m}{s}$]
\mathcal{V}	volume[m^3]
Y^+	dimensionless wall distance[-]
Y_M	contribution of the fluctuating dilatation in compressible turbulence to the overall dissipation rate[$\frac{J}{m^3 \cdot s}$]

1

Introduction

Fuel consumption is a key word in the development of new cars. In a world with limited resources, car manufacturers can no longer ignore the fact that we are depleting our non-renewable resources. Since cars are bluff bodies moving at high velocities they will experience a phenomena known as *drag*. Drag is a resistance force acting against the moving direction. It occurs mainly due to a pressure difference between the frontal area and the wake. Increased drag creates an increased need for power to achieve the same velocity which increases fuel consumption. Therefore, reducing drag is of vital importance.

In late stages of the development process, modification of the product becomes harder and more expensive. Testing these phenomenas with models in a wind tunnel is expensive and impractical in the early stages of the process.

With Computational Fluid Dynamics (CFD) the flow can be analyzed through simulations without needing to perform a full scale physical test. Through these simulations it is possible to create an understanding of how the phenomena causing separation occurs and how changes in geometry can be implemented to reduce drag.

The CFD method has many applications in a variety of fields. Despite it being a fairly new domain, the development of the method has increased rapidly. In automotive aerodynamics, several different studies have been made with the drag coefficient in focus. However, car designers are generally secretive about their findings regarding structural dynamics. This thesis will provide an insight in the flow structure affecting the performance of the car.

1.1 Objective

The project is a numerical study of the flow structure of a Volvo S60 carried out with CFD. Simulations are performed with varying speed, different yaw-angles and a case with and without the antenna. The results are analyzed and explained in this work. The main focus of the project is to understand and present the different flow conditions occurring on the rear of the Volvo S60 under different flow conditions.

1.2 Delimitation

The project is mainly focusing on the importance of a car's geometry, in this case the notchback model with focus on the rear of the car, and will not consider other details. The used terminology for the car sections are described in Figure 1.1 below. The reason for focusing on the rear of the car is because the project is limited to 16 weeks and 5 people which limits the amount of simulations possible to carry out. Simulations are done on a computer restricted by numerical and technical resources. The CAD-model is also a restriction since it is not possible to add new parts other than small simplifications like wheel covers. Some other simplifications in the study are that compared to reality the wind-tunnel is simplified, steady state conditions are applied and the $k-\varepsilon$ turbulence model is used.

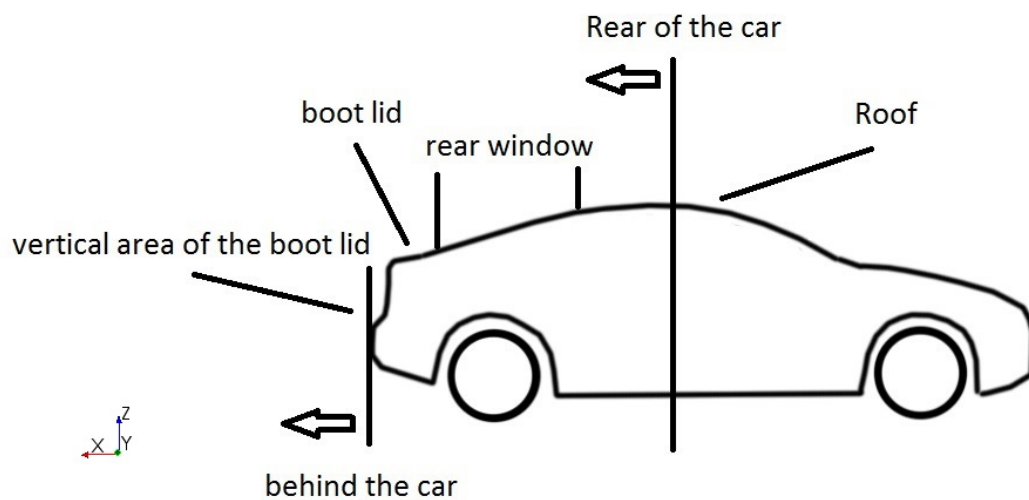


Figure 1.1: Illustrating the terminology used for the car sections.

2

Theory

To fully comprehend the results and conclusion of this report, a theory review for the necessary terminology is provided.

2.1 Fluid Mechanics

In this section of the report a short presentation of the basics of fluid mechanics are presented to give basic knowledge and give more understanding of upcoming parts.

2.1.1 Reynolds number

Taking the dimensionless parameter *Reynolds number* into account while conducting CFD analysis is a must. As the Reynolds law of uniformity states, “Fluid flow passing geometrical identical bodies remain identical if the Reynolds number is equal¹”. This is a usable law when working with scale models and different fluids.

$$Re = \frac{\rho VL}{\mu} = \frac{VL}{\nu} \quad (2.1)$$

As shown in equation (2.1), one can alter the size of the object, velocity of the fluid and the fluid itself, and still keep the same Reynolds number. However, it is essential to keep the Reynolds number constant when using different models and throughout the investigations. The Reynolds number also determines the probability of the flow being laminar or turbulent based on empirical research.

2.1.2 Reynolds transport theorem

One of the fundamental theorems when studying fluid dynamics is *Reynolds transport theorem*. The theorem makes it possible to contemplate a fluid flowing through a system

¹Generally known Reynolds law of uniformity. Alf-Erik Almstedt, 2015, translated from Swedish.

instead of only regarding a fluid particle's path. This system is defined by a *control volume* (C_V). The control volume is an arbitrary volume surrounding the domain of interest and is defined by the *control surface* (C_S), which is an abstract boundary between the control volume and its surroundings. The Reynolds transport theorem enables, with a mathematical model, the system analysis to convert to a control volume analysis. Instead of analyzing individual masses, the mathematics are applied to specific region using the formula:

$$\frac{d}{dt}(B_{syst}) = \frac{d}{dt} \left(\int_{C_V} \beta \rho d\mathcal{V} \right) + \int_{C_S} \beta \rho (\mathbf{V}_r \cdot \mathbf{n}) d\mathbf{A} \quad (2.2)$$

Here B is the property of the fluid and can consist of mass, energy, momentum and angular momentum. $\beta = \frac{dB}{dm}$, is an intensive value, the amount of B per mass unit in any fluid element. \mathbf{V}_r is the relative velocity and \mathbf{n} the normal vector perpendicular to the control surface. This formula describes the alteration of B with respect to time, due to the time dependent alteration of the control volume and flow through the control surface. It may also alter due to different circumstances. For instance, steady flow, compressible and incompressible flow are physics settings that affect the theorem.

2.1.3 Conservation of mass and momentum

As just seen, the Reynolds transport theorem (2.2) can be used for several different operations by varying the variable B . By setting B to mass and combining it with the continuity equation it is possible to derive the equation of mass conservation. From the continuity equation it is self-evident that the inflow of mass minus the outflow of mass equals the change of mass in a system. Thus when the mass of a system is constant, $m_{syst} = \text{constant}$, the outflow will equal the inflow and the derivative of the system will be zero, $dm/dt = 0$. This is used in Reynolds transport theorem and forms the equation of conservation of mass as seen below in equation (2.3).

$$\left(\frac{dm}{dt} \right)_{syst} = 0 = \frac{d}{dt} \left(\int_{C_V} \rho d\mathcal{V} \right) + \int_{C_S} \rho (\mathbf{V}_r \cdot \mathbf{n}) dA \quad (2.3)$$

The linear momentum equation in a control volume can be represented in a similar way. It is commonly known that when a force is exerted on a system the mass will begin to accelerate stated by Newton's Second law.

$$\mathbf{F} = m\mathbf{a} = m \frac{d\mathbf{V}}{dt} = \frac{d}{dt} (m\mathbf{V}) \quad (2.4)$$

When choosing B as $m\mathbf{V}$, thus $\beta = d(m\mathbf{V})/dm = \mathbf{V}$, the Reynolds transport theorem states the linear momentum equation in a control volume.

$$\frac{d}{dt} (m\mathbf{V})_{syst} = \sum \mathbf{F} = \frac{d}{dt} \left(\int_{C_V} \mathbf{V} \rho d\mathcal{V} \right) + \int_{C_S} \mathbf{V} \rho (\mathbf{V}_r \cdot \mathbf{n}) dA \quad (2.5)$$

2.1.4 Boundary layer theory

Currently, three different methods to study external flows can be used; numerical solutions, experimentation and *Boundary layer theory*. Boundary layer theory is developed through simplifications of the *Navier-Stokes equation*:

$$\rho \frac{d\mathbf{V}}{dt} = \rho \mathbf{g} + \nabla \mathbf{p} + \mu \nabla^2 \mathbf{V} \quad (2.6)$$

The left-hand side of the equation describe the force acting on the fluid and consists of the right-hand expressions; gravitational force, the pressure gradient and a stress term due to horizontal friction and shear stress. The consideration of the boundary layer is important as effects within it contribute to the skin friction drag force. Neglecting these forces may lead to incorrect results. The main difference from the bulk flow when analyzing flow close to a surface is that the flow is dominated by viscous forces, compared with being frictionless. A common illustration of the expatiated boundary layer at turbulent conditions is shown in Figure 2.1.

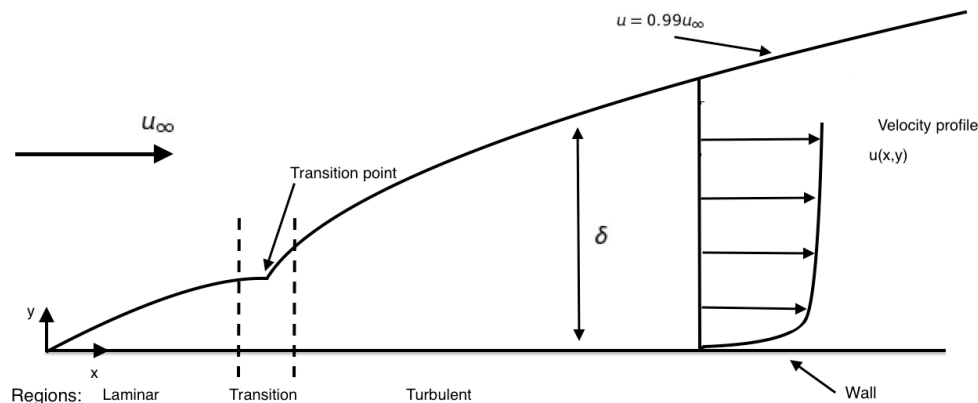


Figure 2.1: Development of the boundary layer at turbulent flow.

The layers can be divided into a few sections, outer layer, buffer layer and viscous sub-layer the closer to the surface one gets. The different velocities in the layers cause friction in the fluid, resulting in shear stress on the surface called *wall shear stress*, τ_w . In the buffer layer there is a mixture of laminar and turbulent shear stress and in the viscous sublayer viscous forces dominates and there are accurate models available.

The development of the boundary layer is highly dependent on the Reynolds number and in vehicle aerodynamics the boundary layer is always turbulent. The boundary layer thickness, δ , is defined as the distance from the ground to that point where the velocity

$u(x,y)$ is 99% of the external velocity, u_∞ . The growth of δ , at a flow along flat surfaces, can be approximated by:

$$\frac{\delta}{x} = \begin{cases} \frac{5.0}{Re_x^{1/2}} & \text{laminar } 10^3 < Re_x < 10^6 \\ \frac{0.16}{Re_x^{1/7}} & \text{turbulent } 10^6 < Re_x \end{cases}$$

2.1.5 Separation

The phenomenon of *separation* is an important part when studying the aerodynamics of cars. Finding the point of separation can be crucial for understanding the appearance of vortices and the contribution to drag. This part will explain the basics behind separation and link it to the study of the Volvo S60.

When explaining separation, it is common to only practice the 2D case and not consider the 3D case. The 3D case is much more complex and it is a field that is not yet completely understood.

Important terms in the study of flow separation are *point of attachment* and *point of separation*. These points are *singular points*, describing interesting phenomena derived to a single point. The point where the fluid connects to the surface is called point of attachment and the point where it disconnects is the point of separation. The separation causes vortices and contributes to drag due to the decreased pressure behind the body, as shown in Figure 2.2.

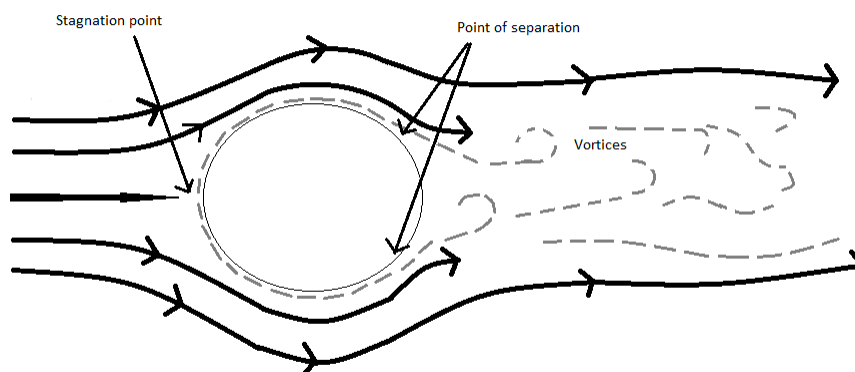


Figure 2.2: Development of vortices due to flow separation.

Due to different pressure gradients, the boundary layer profile takes different shapes, as shown in Figure 2.3. In Figure 2.3 (a), the pressure gradient is smaller than zero, $\frac{\partial p}{\partial x} < 0$.

This is a favourable gradient, from a separation point of view, i.e no separation. When the inflection point comes up from behind the surface and locates exactly at the surface, there is a zero pressure gradient, $\frac{\partial p}{\partial x} = 0$. If the boundary layer profile develops as in Figure 2.3 (b)-(e) due to a pressure gradient larger than zero, the flow is said to have an *adverse* pressure gradient, $\frac{\partial p}{\partial x} > 0$. This does not mean that the flow will separate from the point it becomes zero. The flow in Figure 2.3 (c) is still attached and has an adverse pressure gradient. However, as the wall shear stress, τ_w , becomes zero, the flow reaches a critical adverse pressure gradient and the fluid disconnects from the surface. In Figure 2.3 (d), the flow experience excessive adverse pressure gradient and starts flowing backwards. This is the start of the creation of vortices.

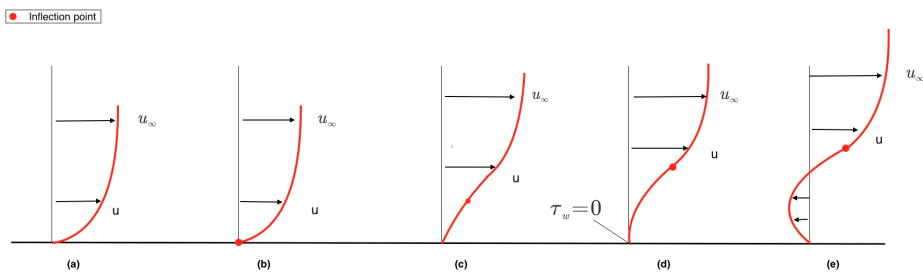


Figure 2.3: Development of boundary layer profiles due to different pressure gradients.

However, this approach will not apply for the 3D case. It is then needed to use more of a phenomenological approach, as the criteria of $\frac{\partial p}{\partial x} > 0$ and $\tau_w = 0$ at the point of separation does not apply.

The phenomena of separation, as stated by Chapman & Yates, owing to three general types of separation [2]; *bubble separation*, *horn separation* and *crossflow separation*. S. Bonitz et al. explain these phenomenons as following [3].

Bubble separation can be described as a separation of different *streamlines* that cannot enter each others regions, where streamlines are lines that illustrate the velocity profile tangential to the line at any given moment. Therefore, there must be various points of attachment on the body to enable reattachment of the flow. Between these attachment points runs the separation line that causes the flow separation, which creates vortices.

Horn separation occurs when the flow recircles the body, forming in to foci and causing vortices. This is a *nodal* singular point and can be seen by limiting streamlines forming a focus with a spiral motion. This type of separation does not generate any isolated regions. Due to this, the fluid can enter at any point on the surface.

A fluid flow that hits a bluff body get convergent streamlines. Due to adverse geometry, the fluid cannot stay attached to the body and separation takes place. This describes the crossflow separation.

2.1.6 Surface pressure coefficient

The *surface pressure* on a car is a very interesting phenomena in the analysis of a car's aerodynamics since it can be used to visualize and explain the different flow conditions occurring on and around a car. It also affects the creation of vortices and the separation making it even more relevant to understand thoroughly.

Not surprisingly, every car has a different pressure distribution since every car has its own shapes. However there are some key features and similarities in cars such as the rear in a notchback model or hatchback model. This makes it quite easy to largely predict the pressure distribution over different cars when studying areas not affected by wake. The pressure distribution largely occurs due to the shapes of the car and the variations in mass flow over the car. Sections exposed to high speeds, and thus a high mass flow, will experience a low pressure and sections exposed to low speeds will experience a high pressure [7]. The pressure exerted on a car will result in what is called a pressure gradient. This is a local characterisation of the pressure in a fluid which occurs due to the variation of mass flow and thus variations in pressure over the car [1].

Studying the pressure distribution in absolute measures often leads to difficulties since the pressure is proportional to the velocity making it increase or decrease depending on the change in velocity. This problem is overcome with the *pressure coefficient*, C_p , which is a coefficient describing the pressure distribution in relative measures instead of absolute.

$$C_p = \frac{p - p_\infty}{\frac{1}{2}\rho_\infty U_\infty^2} \quad (2.7)$$

Here p is the pressure where C_p is being evaluated, p_∞ is the freestream pressure known as the *static pressure*, ρ_∞ is the freestream fluid density and U_∞ is the freestream velocity [1].

With change in speed and yaw angle the pressure distribution will alter. Tests on the DriveAer model show that with small variations in yaw-angles the surface pressure will change slightly [9]. For instance the pressure coefficient will slightly increase on the leeward side on the rear and the rear window of the car since of the decrease in mass flow occurring there and thus a higher momentum will occur [9]. The opposite thing will happen at the windward side. Additionally, this will probably apply to our case when studying the overall pressure distribution.

2.1.7 Vorticity

As earlier stated, the pressure distribution has a large effect on the creation of *vortices*. A vortex is an area in a fluid in which the flow is rotating about an axis line [4]. They occur in fluids that have been perturbed in some way, typically through a stirring motion. The whirlpools forming in the wake of a boat are an everyday example of vortices. Vortices can be characterized and quantified by the use of three variables - *vorticity*, circulation, and the velocity distribution. Vorticity is a vector quantity that describes the local rotary motion at a particular point in the fluid [1]. Mathematically, it is the curl of the velocity field of the fluid i.e.

$$\boldsymbol{\omega} = \frac{1}{2}(\text{curl}\mathbf{V}) = \frac{1}{2} \begin{vmatrix} \mathbf{i} & \mathbf{j} & \mathbf{k} \\ \frac{\partial}{\partial x} & \frac{\partial}{\partial y} & \frac{\partial}{\partial z} \\ u & v & w \end{vmatrix} \leftrightarrow$$

$$w_x = \frac{1}{2}\left(\frac{\partial w}{\partial y} - \frac{\partial v}{\partial z}\right); w_y = \frac{1}{2}\left(\frac{\partial w}{\partial x} - \frac{\partial u}{\partial z}\right); w_z = \frac{1}{2}\left(\frac{\partial v}{\partial x} - \frac{\partial u}{\partial y}\right)$$

If the flow has negligible or zero vorticity, it is called irrotational.

Specifically in relation to cars and aerodynamics, vortices are a pertinent area of study as the rear end geometry of cars has a significant effect on aerodynamic drag [5]. This in turn influences energy consumption, and as shown by Nouwaza et. al [6] vortices can lead to a high drag coefficient value.

It would be reasonable to expect that changes in velocity would lead to changes in the vortex geometries, as the vorticity is simply the cross product of the ∇ operator and the velocity vector.

2.1.8 Q-criterion

The *Q-criterion* is a mathematically-based criterion that can be used to identify vortices. It defines a vortex as a flow region with a positive second invariant of the velocity gradient tensor $\nabla\mathbf{u}$. In order to further explain these terms, some mathematics is needed.

The velocity gradient tensor can be written as $D_{ij} = \frac{\partial u_i}{\partial x_j}$, and since it is a second-order tensor it can be decomposed into a symmetric part and a skew-symmetric (antisymmetric) part:

$$D_{ij} = S_{ij} + \Omega_{ij}$$

where

$$S_{ij} = \frac{1}{2}\left(\frac{\partial u_i}{\partial x_j} + \frac{\partial u_j}{\partial x_i}\right)$$

and

$$\Omega_{ij} = \frac{1}{2} \left(\frac{\partial u_i}{\partial x_j} - \frac{\partial u_j}{\partial x_i} \right)$$

S_{ij} is the strain rate tensor and Ω_{ij} is the vorticity tensor. The second invariant can thus be defined as:

$$Q = \frac{1}{2} (\|\Omega\|^2 - \|S\|^2)$$

According to the Q-criterion, an area is classified as a vortex when $Q > 0$. By this definition, the Q-criterion defines a vortex as an area where the vorticity is greater than the rate of strain.

2.1.9 Skin friction coefficient

Skin friction plays a key role in determining how large the drag force will be, which makes it worthwhile looking in to. The phenomena occurs due to friction effects between the surface of the object and the fluid, in other words the skin friction describes the *wall shear stress*, τ_w . When comparing cases at different velocities, as in this study, it is difficult to analyze the results since skin friction is an absolute measure which means it will change with variation in velocity. This problem is overcome with the *skin friction coefficient* C_f , which measures the wall shear stress in relative measures [1].

$$C_f = \frac{\tau_w}{\frac{1}{2}\rho U_\infty^2} \quad (2.8)$$

2.1.10 Aerodynamic forces

When talking about automotive aerodynamics and pressure distribution, two different forces are often mentioned; the *lift/downforce* and the *drag force*. If the pressure gradient is directed up it will thus create a force directed up, which is what is called the lift force F_L . If the pressure gradient is directed the opposite way, down, it will generate a force that forces the car down called downforce D [1]. The other force worth mentioning is the drag force F_D which is a result of the pressure gradient combined with skin friction. *Pressure drag* F_P occurs when the pressure gradient is directed horizontally, instead of vertically as in lift and downforce, and *friction drag* F_F occurs due to friction effects between the surface of the object and the fluid [1]. The sum of these two are what is called the drag force.

$$F_D = F_P + F_F \quad (2.9)$$

The lift and drag force each have coefficients called C_L and C_D , which are defined as

$$C_D = \frac{F_D}{\frac{1}{2}\rho U^2 A} \quad (2.10)$$

$$C_L = \frac{F_L}{\frac{1}{2}\rho U^2 A} \quad (2.11)$$

Following, (Figure 2.4), shows the different mentioned forces and its directions.

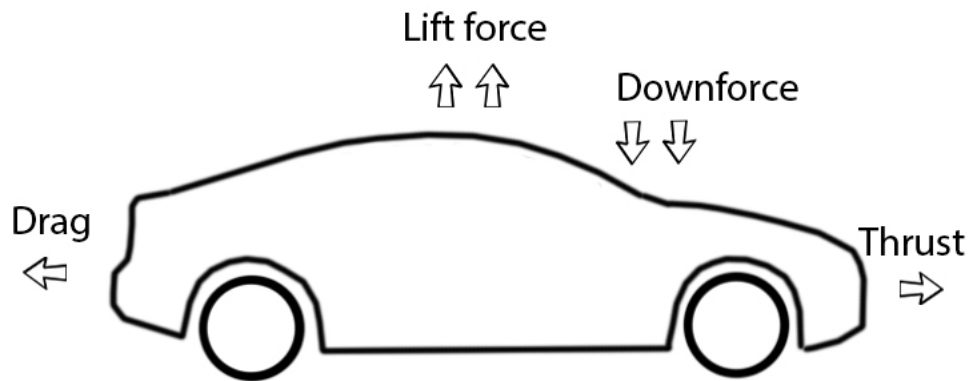


Figure 2.4: Directions of drag, lift, downforce and thrust.

2.1.11 Yaw angle

The angle between the driving direction of the vehicle and the air hitting the car while still flowing parallel to the ground is known as the *yaw angle*, see Figure 2.5.

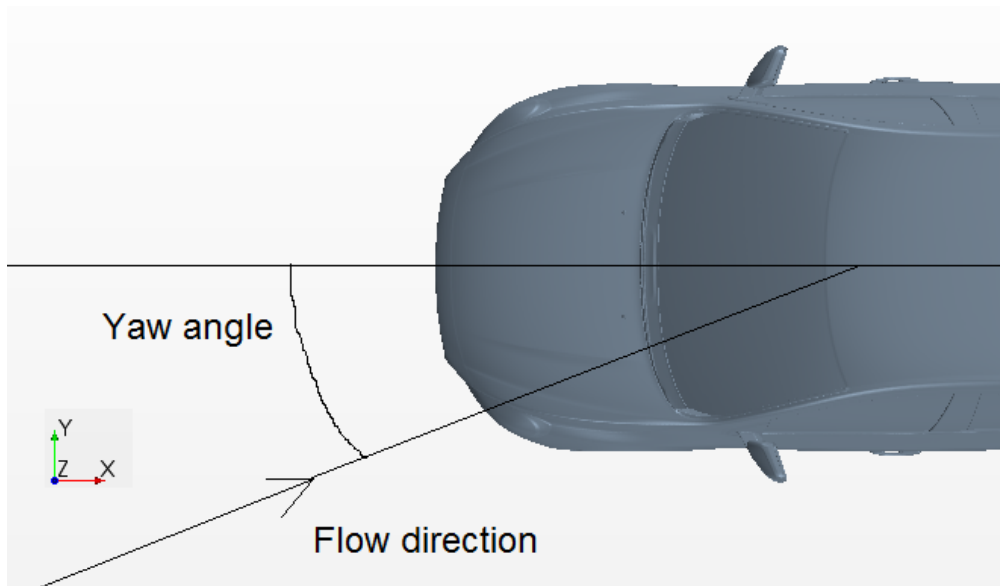


Figure 2.5: Illustration of the yaw angle.

When the flow changes, there is a certain time delay before the wake behind the car changes. The result of this is that the side force the airflow creates, momentarily reduces, but the momentum will increase during this time delay [14].

Higher turbulence in the airflow reduces the vehicles sensitivity to yaw angle changes, but it does increase the total drag force. Sudden changes in the yaw angle, e.g while overtaking another vehicle, creates an asymmetry in the air flow and increases the momentum from the side forces and also increases the drag and lift force on the vehicle.

The drag and lift coefficient and the yaw momentum changes when the velocity of the flow and/or the yaw angle changes. The lift and drag coefficients varies heavily with the shape of the vehicle, even if the body of the vehicles seems to be almost the same the differences in lift and drag will be substantial [15].

2.2 Computational Fluid Dynamics

CFD is the abbreviation for Computational Fluid Dynamics and is a method used to simulate flows using computational hardware. This means CFD can be used to study for instance how fluids interact with multiple flows and how fluids interact with solids. From these studies it is then possible to determine characteristics like how the velocity and pressure develop in the studied domain.

The CFD method is mainly used since it is faster and less costly than doing full scale experiments [10]. Most software using the CFD method are able to automate the simulation process meaning they can do thousand of runs to find optimal results without needing to much interaction with an operator.

In this section fundamental parts of the theory behind the CFD software STAR-CCM+ will be explained.

2.2.1 The finite volume method

Many CFD programs base their computations on *the Finite Volume Method* (FVM). The FVM is a discretization technique used for evaluating partial differential equations (PDEs), particularly those that arise from the physical conservation laws (e.g. continuity, momentum, energy) [19]. FVM is used widely both in industry and academia, particularly in fluid mechanics. It owes its popularity to its simplicity and its ability to model unstructured meshes.

In a similar fashion to the Finite Element Method, it calculates values at computational nodes on a meshed geometry. The FVM gets its name from the way the mesh is constructed; it divides the domain into non-overlapping control volumes, cells, where the PDEs can be integrated [20]. The computational nodes are found at the centroid of

each C_V . The algorithm of a CFD program generally comprises the following steps:

- Integration of the governing PDEs of fluid flow over the control volumes of the considered domain
- Discretization which involves the substitution of approximations for the quantities in the integrated PDE which accounts for flow processes such as convection, diffusion and conduction. This process transform the integral into an algebraic equation system.
- The algebraic equation system can now be solved by an iterative method e.g. Euler's forward or backward schemes, or the Crank-Nicholson scheme.

A characteristic and advantageous feature of the FVM is that it produces a conservative solution, which can be proven to converge [21]. A detailed mathematical analysis of the Finite Volume Method is beyond the scope of this text. For further clarification, the reader is encouraged to consult [20].

2.2.2 Turbulence modelling

Turbulence is practically unavoidable while investigating the flow around a bluff body such as a car. When modelling turbulence the instantaneous variables are usually decomposed into a mean value and a fluctuating value

$$u_i = \bar{u}_i + u'_i, \quad v_i = \bar{v}_i + v'_i, \quad w_i = \bar{w}_i + w'_i, \quad p = \bar{p}_i + p'_i, \quad (2.12)$$

One reason for decomposing variables is that when the flow quantities are measured the point of interest is usually the mean values rather than the time histories. Also when solving the Navier-Stokes equations numerically, it would require a very fine mesh to resolve all turbulent scales and a fine resolution in time. This demands a lot of computer resources and time. To reduce the complexity of the calculations Reynold's time-averaging concept (presented in Reynolds-Averaged Navier-Stokes) is used to lower the complexity and demand for computational resources, for time-averaging to be valid the simulations assume steady-state [11]. The refinement to the wall is crucial for obtaining a high resolution grid thus making an accurate simulation.

Laminar/turbulent

A *laminar flow* is a flow where a fluid flows close to a surface where the viscous force is the dominant force. A laminar flow usually has a low velocity and a low Reynolds number. With higher velocity the Reynolds number increases, and the flow will start going into a turbulent state if the values of the velocity gets high enough [12].

A turbulent flow has a highly irregular flow, which occurs due to instabilities and changes

constantly in time. Turbulence is sometimes a wanted phenomenon and sometimes unwanted. When it comes to aerodynamics of any kind of moving vehicle, turbulence increases the drag coefficient on the vehicle and if powerful enough turbulence can cause the vehicle to be unstable and have poor handling qualities [13].

Reynolds-Averaged Navier-Stokes

As earlier stated due to the rapid changes in turbulent flow, simplifications have to be implemented to be able to model turbulent flow. One approach is to divide the variables velocity, pressure and shear stress into two parts, a *time-averaged part* \bar{u} and a *fluctuating part* u' . This is what is known as *Reynold's Time-Averaging Concept* and is shown for the velocity below.

$$u(x,y,z,t) = \bar{u}(x,y,z,t) + u'(x,y,z,t) \quad (2.13)$$

By time averaging the Navier Stokes equations the *Reynolds-Averaged Navier-Stokes (RANS)* are obtained

$$\rho \bar{u}_j \frac{\partial \bar{u}_i}{\partial x_j} = \rho \bar{f}_i + \frac{\partial}{\partial x_j} \left(-\bar{p} \delta_{ij} + \mu \left(\frac{\partial \bar{u}_j}{\partial x_j} + \frac{\partial \bar{u}_j}{\partial x_i} \right) - \overline{\rho u'_i u'_j} \right) \quad (2.14)$$

With this rewriting the Navier-Stokes equations can be solved for a turbulent flow. Depending on the turbulence model in question the last term $\overline{\rho u'_i u'_j}$, known as the *Reynolds stress* is determined differently. A more thorough explanation can be found in [1].

k- ε model

There are several different models to approximate turbulent flow. A commonly used model is the *k- ε model* which is a model based on the RANS equations (2.14). By taking different forms depending on the application and predicted y^+ values it can be used for different applications. In this case the realizable k- ε two layer model is used. It is suitable since it has a certain robustness for this application. This turbulence model differs from the standard realizable k- ε model by including two extra equations to solve the transport equations for the *turbulent kinetic energy* k and its *dissipation rate* ε . As a result of this and by using a two layer approach, the model will provide more precise results of the spreading rate of round and planar jets. The model uses what is called the *Boussinesq-assumption* to calculate the Reynold stress shown below:

$$\overline{u^2} = \frac{2}{3}k - 2\nu_t \frac{\partial U}{\partial x} \quad (2.15)$$

where ν_t is calculated μ_t/ρ . μ_t is called the *turbulent viscosity* and is calculated by using k and ε :

$$\mu_t = \rho C_\mu \frac{k^2}{\varepsilon} \quad (2.16)$$

Here C_μ is a structure constant depending on the conditions. This combined with the two transport equations for k and ε shown below is what is used to model turbulent

flow.

$$\frac{\partial}{\partial t}(\rho k) + \frac{\partial}{\partial x_j}(\rho k u_j) = \frac{\partial}{\partial x_j} \left(\left(\mu + \frac{\mu_t}{\sigma_k} \right) \frac{\partial k}{\partial x_j} \right) + G_k + G_b - \rho \varepsilon - Y_M + S_k \quad (2.17)$$

$$\frac{\partial}{\partial t}(\rho \varepsilon) + \frac{\partial}{\partial x_j}(\rho \varepsilon u_j) = \frac{\partial}{\partial x_j} \left(\left(\mu + \frac{\mu_t}{\sigma_\varepsilon} \right) \frac{\partial \varepsilon}{\partial x_j} \right) + \rho C_1 S \varepsilon - \rho C_2 \frac{\varepsilon^2}{k + \sqrt{\nu \varepsilon}} + C_{1\varepsilon} \frac{\varepsilon}{k} C_{3\varepsilon} G_b + S_\varepsilon \quad (2.18)$$

$$C_1 = \max \left(0.43, \frac{\eta}{\eta + 5} \right), \quad \eta = S \frac{k}{\varepsilon}, \quad S = \sqrt{2 S_{ij} S_{ij}} \quad (2.19)$$

A more thorough explanation on how these equations are formed can be found in [17] and [18]. All constants are defined in the nomenclature in the beginning of the report.

Wall treatment

When in the *boundary layer*, dimensionless units are used. The distance from the wall to the stream velocity is called, y^+ , and the fluid velocity parallel to the wall is called, u^+ . The shear velocity or friction velocity, u^* , is a shear stress re-written in units of velocity [1].

$$u^+ = \frac{u}{u^*}$$

$$u^* = \sqrt{\frac{\tau_w}{\rho}}$$

$$y^+ = \frac{y u^*}{\nu}$$

These units are important in boundary layer theory and defining the “law of the wall” [1].

$$\frac{u}{u^*} = \frac{1}{\kappa} \ln \frac{y u^*}{\nu} + B$$

The law of the wall is valid for turbulent flow, when in the overlap layer, and approximately constant shear stress. In the wall layer, u^+ can be seen as equal to y^+ thus linear from the wall up to $y^+ \leq 5$. At $y^+ \geq 30$ the logarithmic law and the overlap layer starts, as seen in 2.6.

When simulating it is important to select a wall treatment suitable for the turbulence model and case at hand to satisfy specific y^+ value. The wall treatment used in this project performs three important functions.

- Specifies the reference velocity u^* to be used in the wall laws
- Computes a special value of turbulent production G_k in the wall cells
- Computes a special value of turbulent dissipation ε in the wall cells

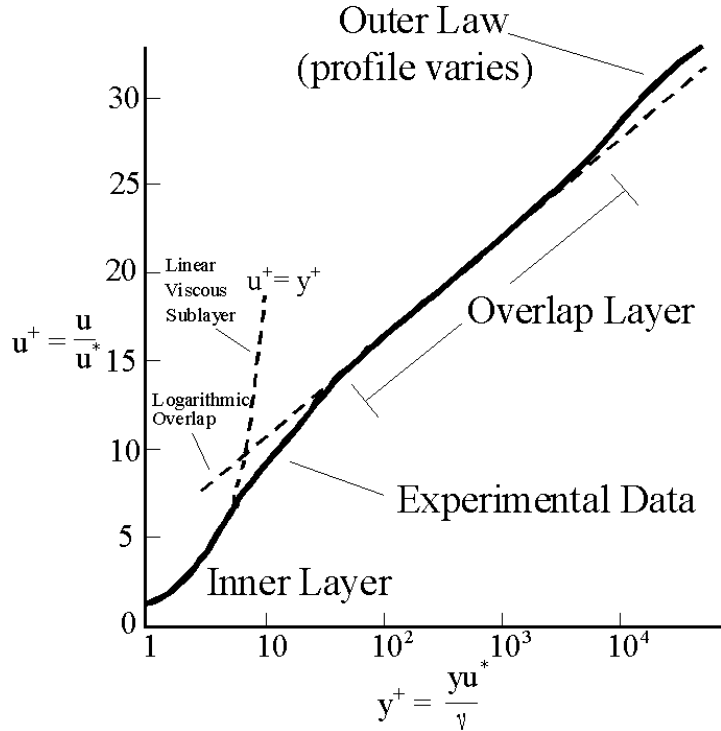


Figure 2.6: Plot of u^+ and y^+ for boundary layer at turbulent flow[24].

The wall treatment used is “Two-Layer All y^+ Wall Treatment” which is identical to the “All y^+ Wall Treatment” but contains a wall boundary condition for ε that is consistent with the two-layer formulation. The wall treatment gives results similar of low y^+ and high y^+ wall treatment when $y^+ \rightarrow 0$ and $y^+ > 30$ [16]. The all- y^+ wall treatment is a good all-round choice for complex geometries such as in this project when a coarse mesh is needed to avoid long simulation time and when it will be difficult to reach low y^+ values. All y^+ is used since there will be regions on the car with different fluid velocity and STARs-CCM+ will use the most appropriate treatment depending on the y^+ .

When simulating flows and there is a need to capture the flow field in the near-wall region it is recommended to use prism layers. When implemented there must be a sufficient amount of prism layers combined with a smooth cell size transition to solve the prism layer total thickness that covers the boundary layer on a wall. The number of prism layers required and their height, depend on the type of flow and physics selected.

For turbulent flows the number of prism layers required to solve the boundary layer, while the first cell height is within acceptable y^+ values, is determined by which wall treatment is selected.

- For "High y^+ " wall treatment, which is similar to two-layer all y^+ , 1–2 prism layers

can be sufficient as long as the near wall cell is being maintained at y^+ values varying from 30 to 300.

- For a “low y^+ ” wall treatment, 10-20 prism layers may be required, but the y^+ must be around 1 which can be difficult to achieve with a complex geometry.

2.2.3 Compressible and incompressible flow

Simulations and calculations on fluids can be solved either with *compressible* or *incompressible flow*. Incompressible flow simplifies and saves time since it removes a varying variable by implying that the fluid in question has a constant density over time and space. There are some cases when it is possible to approximate a fluid with incompressible flow even though there is a compressible flow. This is valid when the so called *Mach number* is below 0.3. The Mach number is defined as

$$Ma = \frac{V}{a} \tag{2.20}$$

Here V is the local flow velocity and a the speed of sound. The Volvo S60 has a Mach number that is less than 0.3 and thus calculations will be done with the setting constant density (incompressible flow).

3

Method

This section describes the method used to analyse the Volvo S60. The project consists of three major parts; literature review, CFD-simulation and post-processing.

3.1 Literature Review

The project started with a literature review to gain more knowledge about vehicle aerodynamics. Every team member looked into different fields which they later presented to the team to learn as much and work as effectively as possible. The various parts of the car were used as the foundation of the literature study; this included parts such as the rear, the spoilers, the mirrors, the wheels and the front. Additionally, many physical phenomena were studied in tandem with the car parts; examples of such phenomena were vortices, separation and pressure, which are presented in the theory part of the report. The main database used in the literature study was SAE. Google scholar and course literature were also searched through but no information of significance was found from these sources. The study found that the most meaningful area in terms of drag reduction lay in the rear of the car, as well as the area that exhibited the most interesting physical phenomena. The literature study laid the foundation for the next step, the simulation.

3.2 CFD and STAR-CCM+

The CFD-part consists of pre-processing, solving and post-processing. The steps needed to set up a simulation are preparation of the geometry and setting up boundaries, mesh generation and setting up physics and solver settings. The version of STAR-CCM+ used is 10.04.011. Following are the steps and the settings used.

3.2.1 Geometry preparation and setting up boundaries

When working with CFD the starting point is usually a CAD model. In this bachelor thesis, an already wrapped CAD model was provided. This means the geometry was already prepared with closed surfaces. To better simulate the real wind tunnel scenario wheel covers were added to the rims. The antenna was removed for the Reynolds study to make it more interesting and unique. Removing the antenna also allowed for the comparison between cases with and without the antenna.

After the geometry preparation, the wind tunnel and car were set up with boundaries; the three types of boundaries used were velocity inlet, pressure outlet and symmetry wall. With the boundary types defined, the mesh settings were defined.

3.2.2 Mesh generation

The mesh settings play a key role in determining the quality of the mesh and thereby, the accuracy of the solutions. The values for the mesh on the exterior were set according to Table 3.1 below.

Table 3.1: Settings for the exterior mesh.

Exterior	
Target surface size	8 mm
Minimum surface size	2 mm
Surface curvature	360 pts/circle
Gap closure size	3 mm

Custom controls override any of the default controls for the surface mesh; this allows the mesh to be refined or coarsened in specific areas as seen fit. Custom controls were utilized in the mesh over the A-pillar, handles and antenna since these are areas where the presence of physical phenomena such as acceleration or vortices necessitated a more refined mesh. An example for the custom controls for the A-pillar is given in Table 3.2.

Table 3.2: Settings for the A-pillar mesh.

A-pillar	
Target surface size	2.0 mm
Minimum surface size	0.5 mm
Surface curvature	360 pts/circle

The fluid volume meshing controls the mesh for the fluid, air in this case, as opposed to the mesh for the physical object, the Volvo S60. The surface growth rate specifies the rate at which face edge sizes vary from one face to an adjacent one. The number of prism

layers used was 3. This was seen as an adequate value in terms of providing an accurate solution within a reasonable computational time. Prism layer stretching sets the rate at which successive prism layers grow, and the total thickness controls the overall thickness of the prism layers. The maximum cell size limits the largest cell size so that the mesh does not grow too coarse. These determine the accuracy of the results of the simulation and more importantly they play a key role in determining whether the simulation will provide any solution at all. The settings for the fluid volume meshing are presented in Table 3.3 below.

Table 3.3: Settings for the fluid volume mesh.

Fluid volume meshing settings	
Target surface size	8 mm
Minimum surface size	3 mm
Surface curvature	360 pts/circle
Surface growth rate	1.3
Number of prism layers	3
Prism layer stretching	1.3
Prism layer total thickness	7 mm
First cell size	1.8 mm
Maximum cell size (WT wall)	320 mm

Some alteration was made to the 80 kph Reynolds dependency case, to obtain suitable y^+ values. The changes that were made included: changing the total thickness of the prism layer to 8 mm and using wall thickness as the distribution mode. The value for the first cell height was set to 2 mm.

Refinement settings were made for areas of interest to get a more explicit solution. This was done by reducing the cell size and increasing the cell numbers. These alterations can result in convergence problems, but in this particular case it worked well. The following figure, Figure 3.1, shows the different refinements.

When generating a mesh it is not unusual that a few invalid cells are created. The problem with these cells are that they have some kind of defect, e.g. a negative volume, which disrupts the computations. STAR-CCM+ has a built in tool to identify the cells that do not meet the cell quality conditions. This was used every time the mesh was updated with the conditions shown in Table 3.4 below.

Generally, this should remove the issues regarding cell-quality. However, in some cases all invalid cells were not detected and thus when running the simulation these cells caused divergence or an acceleration of the velocity to infinity, which thus made the solution

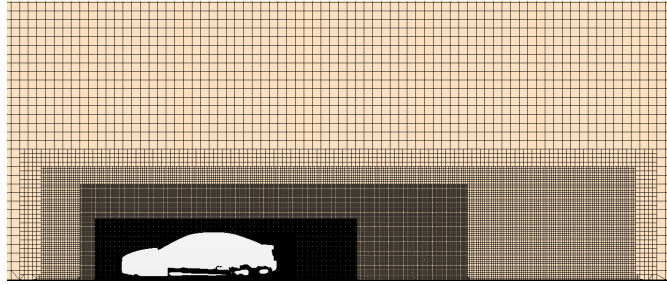


Figure 3.1: Mesh refinements.

Table 3.4: Settings used for removing invalid cells.

Cell quality conditions	
Face validity	< 0.95
Cell quality	< 1E-5
Volume change	< 1E-4
Contiguous cells	< 100
Connected face area	< 1E-8
Volume	< 0

invalid. This was corrected by identifying the cells, removing them and running the simulation once more. The number of cells for the Reynolds dependency cases were 48.3 million, and 48.5 million cells for the yaw angle cases.

3.2.3 Setting up physics and solver settings

Setting up the physics is a crucial part of pre-processing since the physics are the mathematical models used by STAR-CCM+ to solve the simulation and thus model the reality. The physics used in this bachelor thesis are summarised below. More thorough explanations of each model can be read in the theory part of the report.

- Cell quality remediation
- Constant density
- Coupled density
- Gas
- Gradients
- k- ϵ model
- Realizable k- ϵ two-layer

- Reynolds-Averaged Navier-Stokes
- Steady
- Three dimensional
- Turbulent
- Two layer all y^+ wall treatment

The solver settings used were the default settings for this application. Most of the time these settings together with the settings shown below were enough to make the simulations converge in about 10 000 to 15 000 iterations.

Table 3.5: Settings for solver.

Solver settings	
Courant number	30
Minimum explicit relaxation	0.01
Minimum relaxation factor	0.6

When the simulations closed in on 15 000 iterations without showing potential of a good enough solution or a slow converging speed, settings were changed. Two important settings that contributed to convergence and more exact solutions were the Courant number and the minimum explicit relaxation. Depending on the value of the Courant number fluid particles move through a number of cells each time step. By increasing the value, in this case from 30 to 40, the fluid particles thus move through more cells each time step. This made the simulations with slow convergence faster and finish within 2000 more iterations.

The minimum explicit relaxation sets the minimum scale by which the correction controls optimizes the solution for each iteration. This means that by lowering the value, in this case from 0.2 to 0.01, the solution will converge slower but with a more precise solution. This was used together with lowering the Courant number in cases where a good enough solution was not achieved.

3.2.4 Setting up the yaw conditions

The yaw angle was also varied in order to examine the impact of a varying yaw angle on the flow structure and various properties such as pressure. For these yaw simulations, the velocity was kept constant at 100 kph and they were done with the antenna.

As explained in the theory section, the yaw angle is the angle between the direction of travel of the car and the angle of incidence of the air. This was modelled in STAR-CCM+ by setting one of the wind tunnel walls to a velocity inlet as well as specifying

a number for the desired yaw angle. The opposite wall was set to a pressure outlet. Additionally, the wind tunnel was widened by a factor of 1.5 on both sides in order to account for the wake, created by the angled flows. Otherwise, the settings for the yaw simulations were similar to the settings discussed above.

3.2.5 Convergence

To see if the simulations converged the residuals and drag coefficient were monitored. When the residual for turbulent dissipation rate (TDR) was below 0.001 and the C_D was constant, only fluctuating with one *drag count*, one thousandth part of the C_D value, the simulation was said to be converged. Even if the TDR residual was above the limit but C_D was still constant the simulation was considered to be converged. It should be noted that other parameters such as continuity, momentum in x,y,z and turbulent kinetic energy were also monitored, however these were not as heavily followed as these parameters were generally very low. Since C_D is supposed to be the same for a object at different velocities this was also a way of checking for convergence. Therefore if the C_D for a simulation converges to the same value as an old simulation it was assumed to be converged. However, it should be noted that for many configurations C_D can vary and as a result it was used in conjunction with the residuals to determine convergence.

3.3 Investigated Cases

The cases investigated can be divided into three categories: Reynolds dependency, yaw angle and antenna comparison. The Reynolds dependency cases were intended to investigate the effect of varying velocity on certain properties such as skin friction or pressure. The yaw angle cases examined the impact of a varying yaw angle (the configuration for the angled flow is shown Figure 2.5). Finally, the antenna comparison was meant to showcase how the antenna impacts the flow structure of the car. The investigated cases that were chosen for analysis are shown below:

- Reynolds dependency: 80 kph, 100 kph, 120 kph, 140 kph and 200 kph.
- Yaw angle: 0°, 2.5°, 5° and 10°.
- Antenna: 100 kph with antenna and 100 kph without antenna.

3.4 Post-processing

The post-processing was initialized by extracting pictures and visual data from STAR-CCM+. This was performed for the different velocities and yaw angles. Finally, these pictures were analysed by observing the occurring physical phenomena and comparing these to the theory.

4

Results and Analysis

This section presents the results obtained from the CFD simulations in graphical form as well as providing an analysis of the observed phenomena. Initially the Reynolds dependency study is discussed, followed by the antenna study and finally the yaw angle study. The validity of CFD simulations and y^+ is also considered.

4.1 Validation of Simulations

As CFD simulations are estimations of reality, one can question the accuracy and the validity of the results. The simulations are done with some, earlier mentioned, simplifications and models to interpret conditions experienced in reality. Worth mentioning is that neither CFD simulations nor wind tunnel testing are scenarios fully representable of real life driving experiences. These are merely acceptable scenarios representing the real world and CFD/wind tunnel results can not be compared with the real world.

With assistance and results from a wind tunnel test, provided by S.Bonitz, the results from the CFD simulations could be evaluated. For further information about the wind tunnel testing, see [3], [8].

Since this study was focused on the rear of the car, and such results could be obtained from the wind tunnel testing, this section will generate a comparison between the wind tunnel test and the CFD simulations. This was executed by looking at the rear window and the area behind the antenna at 100 kph. As Figure 4.1 and Figure 4.2 illustrate the surface pressure distribution, it can be seen that the structure is fairly similar. Flow structure similarities are shown with paint visualization from the wind tunnel and surface vectors from the CFD, illustrated in Figure 4.3. Figure 4.1(a) and Figure 4.1(b) both show two distinct areas of higher pressure coefficient at the bottom-side of the window and the overall pattern of build-up is equal. The same goes for the antenna

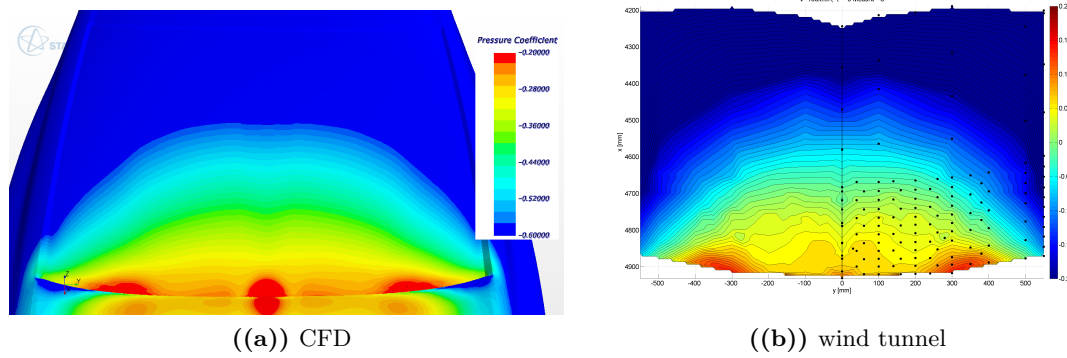


Figure 4.1: CFD and wind tunnel comparison of the surface pressure distribution over the rear window.

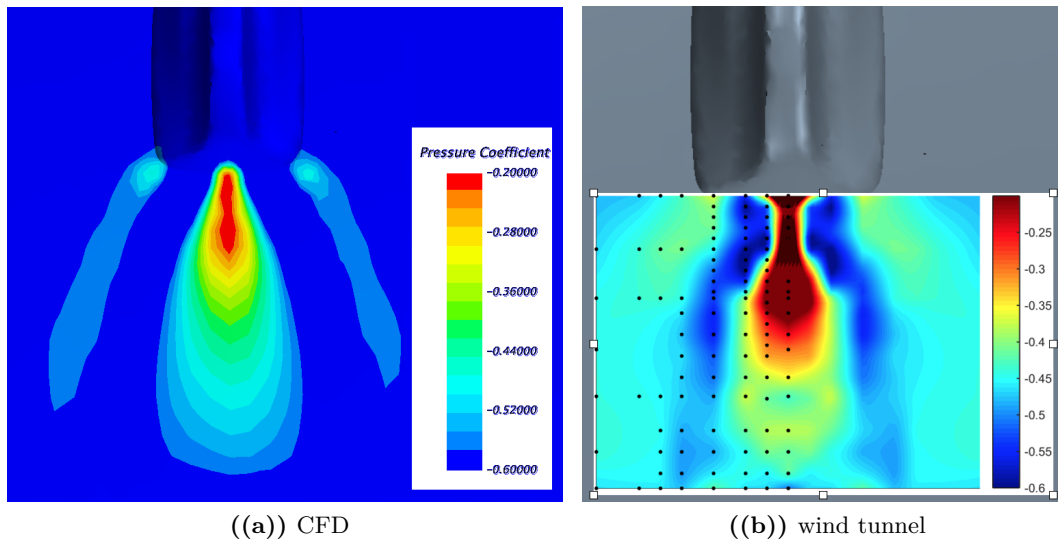


Figure 4.2: CFD and wind tunnel comparison of the surface pressure distribution at the Antenna.

in Figure 4.2, with regards to structural uniformity and distinct areas of high and low pressure coefficient placed in the same way.

This comparison indicates that the simulations produced in Star CCM+ are comparable to the wind tunnel tests, i.e the results from the CFD simulation are valid.

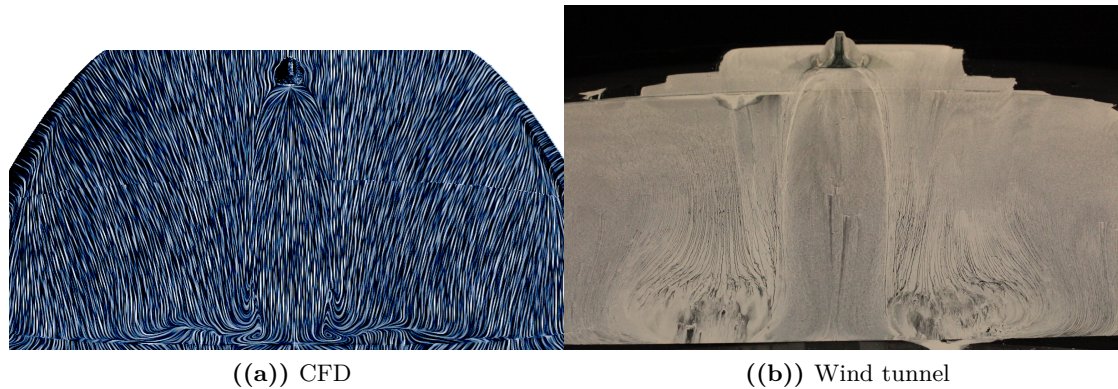


Figure 4.3: Paint visualization in wind tunnel compared with vector representation in CFD.

4.2 Valid y^+ Values

Since the Two-Layer All y^+ wall Treatment was used, the solutions were only valid when the y^+ values ranged from 30 to 150. A study of the surface y^+ scenes showed that for most regions of the car this applied, though with some exceptions. The scenes for the y^+ studies are presented in Appendix A.

One area of the car which had a low y^+ area was the vertical side of the boot lid, but this was said to be acceptable since this was not an area of interest and does not affect the phenomena of relevance occurring on the car. Another area with low y^+ was the area between the window and boot. The reason for this is the low velocity, and was tolerated since it was an area of negligible size. An overall finding was that with higher velocity the y^+ values increased.

The conclusion from the y^+ scenes was that the areas of interest were in the right value range and therefore fulfilled the requirement for the selected wall treatment. Finally, worth noting is that the y^+ treatment functions also help to reduce errors in the low y^+ areas, thus improving remaining small areas with low y^+ values. Consequently the simulations were valid.

4.3 Reynolds Dependency

This section will examine and analyze the results to see if there is a Reynolds dependency. As established previously, the velocities used were 80 kph, 100 kph, 120 kph, 140 kph and 200 kph. The flow structures of these cases will be analyzed with respect to certain physical properties, in order to find a relation between increasing velocity and physical properties.

4.3.1 Drag coefficient

The drag coefficient values are almost constant for the different velocities, seen in Figure 4.4 below. The numerical values for the drag coefficient are also shown in Table 4.1.

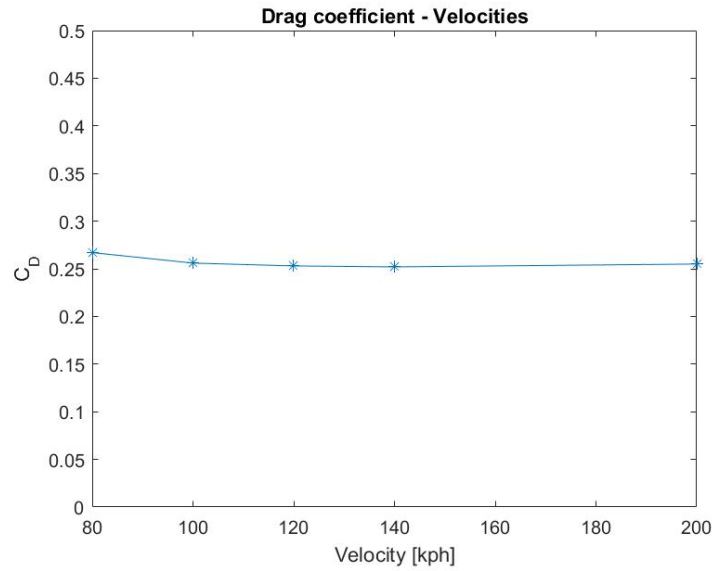


Figure 4.4: Graph of drag coefficient vs. velocity.

Table 4.1: Drag coefficient values for the different velocities.

Velocity [kph]	C_D
80	0.267
100	0.256
120	0.253
140	0.252
200	0.255

As mentioned in the convergence section 3.2.5, the drag coefficient is the same for an object at different velocities. When looking at the drag coefficient values for the car, they were almost identical. The small differences could be due to uncertainties in the simulations. However, the drag coefficient only varies for one drag count and this gives a deviation that is insignificant. An interesting observation is that C_D for 80 kph is higher, compared to the other variances. It might be because of the different prism layer settings made in the case. These settings are can be found in section 3.2.2.

4.3.2 Surface pressure coefficient

For all five cases the pressure zones placements remain fairly similar, as seen in Figure 4.5. Though, it is worth noting that the actual dynamic pressure does still increase. The distribution is characterized by three areas at the bottom of the rear window; a main area in the middle and one on each side of the middle. However, Figure 4.5 shows some variation in pressure distribution and limiting streamlines which will be investigated below. The surface pressure coefficient for all different velocities investigated can be seen in appendix B.

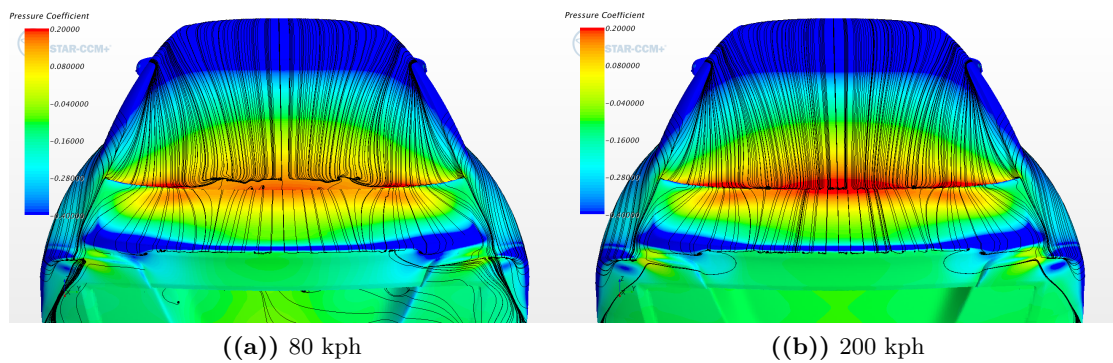


Figure 4.5: Surface pressure coefficient for 80 and 200 kph.

The main pressure coefficient area at the bottom of the rear window can be explained by studying the limited streamlines and the geometry over the rear window and boot lid. Figure 4.6 shows a high velocity over the roof, which is an indication of an attached flow.

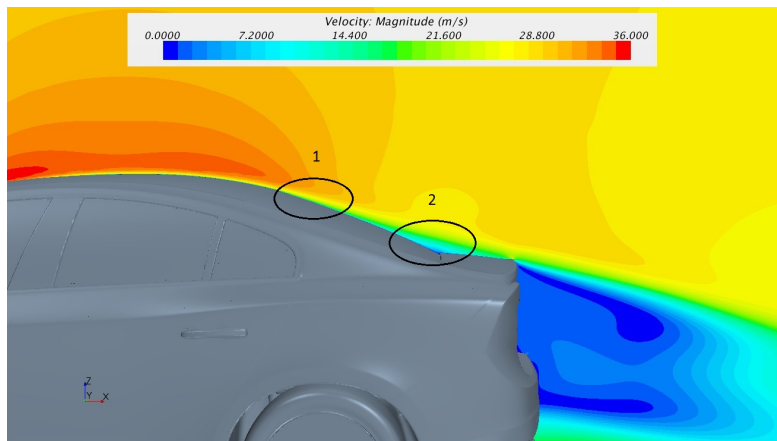


Figure 4.6: Velocity on a symmetry plane at 100 kph.

The streamlines over the roof are spread out, covering the whole width of the roof and show a uniform flow. As these travel over the rear window they start converging. At the bottom the streamlines are more concentrated to an area in the middle of the rear window. When the flow reaches this area the gap between the window and the boot lid causes the flow to stagnate, which is what could be the explanation for the high pressure area occurring there.

The other two high pressure coefficient areas are a bit harder to explain. However, they do indicate a flow that stagnates at the transition from the rear window to the boot lid as there is a high pressure area. Another interesting observation at the same area is seen when visualizing the Q-criterion over the rear window and boot lid. Figure 4.7 shows that there is one vortex travelling above each of the high pressure areas. A complementary investigation of the flow structure occurring here is given in section 4.3.3

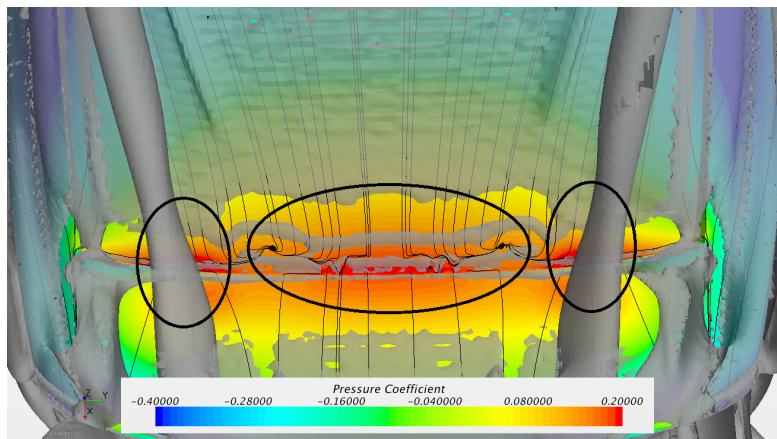


Figure 4.7: Q-criterion with isovalue 100 over the surface pressure coefficient at 100 kph.

Directly after, the flow accelerates again and the pressure over the boot lid starts to gradually decrease, which can be seen in the Figure 4.8.

Because of the wake created behind the car, there is a low velocity and low pressure area on the vertical area of the boot lid as can be seen in Figure 4.5(a) and 4.6. The wake is created due to the flow separating at the rear edge of the boot lid, since it can not follow the body of the car, thus creating a wake.

As mentioned, the limiting streamlines travelling over the roof, converge when flowing over the rear window. As the streamlines are converging in to several foci at the bottom of the window, seen in Figure 4.8, the flow separates according to horn separation. An interesting observation is that the streamlines are pulling away from the high pressure areas at the bottom window. Similar observations were made by S.Bonitz et.al

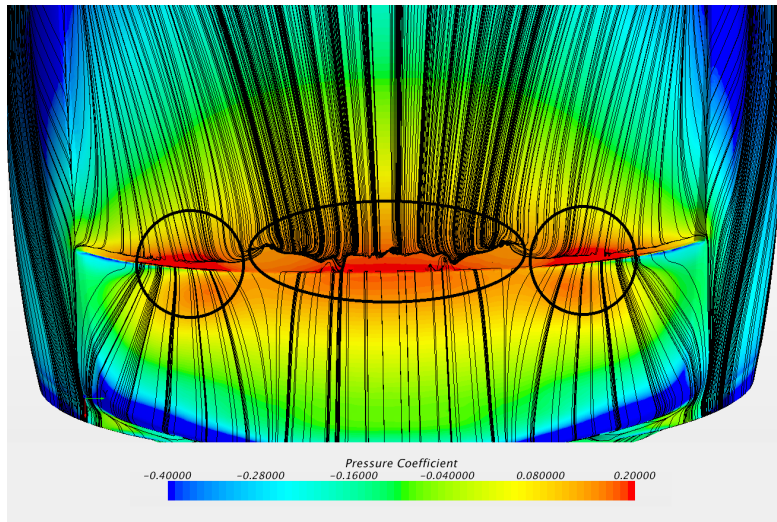


Figure 4.8: Pressure coefficient with streamlines at 100 kph.

in [8]. The streamlines from the centre are pulling towards the sides and the streamlines from the sides are pulling towards the centre.

As stated earlier the pressure zones placement stay similar relative to each other. In the 200 kph case the area in the middle of the rear window, the surface pressure coefficient is higher than in the 80 kph case, though still acting in the same area. Another observation is that in the 200 kph case, the streamlines reach further down the back window, which does suggest that more air gets stuck in the gap and therefore there is an increase in pressure.

4.3.3 Skin friction coefficient

All of the cases exhibit a range of extreme values for the skin friction coefficient. Using the 100 kph case seen in Figure 4.9 as an example, some areas over the back of the car distinguish themselves by showing extreme values, either high or low.

High skin friction coefficient

Over the C-pillar, at the transition from the roof to the rear and on the trailing edge of the back lid, the skin friction coefficient is high. This indicates an attached flow, with high skin friction.

Over the C-pillar, the high skin friction coefficient is due to an attached flow that accelerates over the C-pillar. At the transition from the top of the C-pillar to the rear window the flow converges and accelerates over the radius, as seen in Figure 4.10(a) and Figure 4.10(b). This theory can be strengthened by analyzing the Q-criterion and the vorticity in the x-direction. A vortex passing this area of interest, can be traced to initiate at the

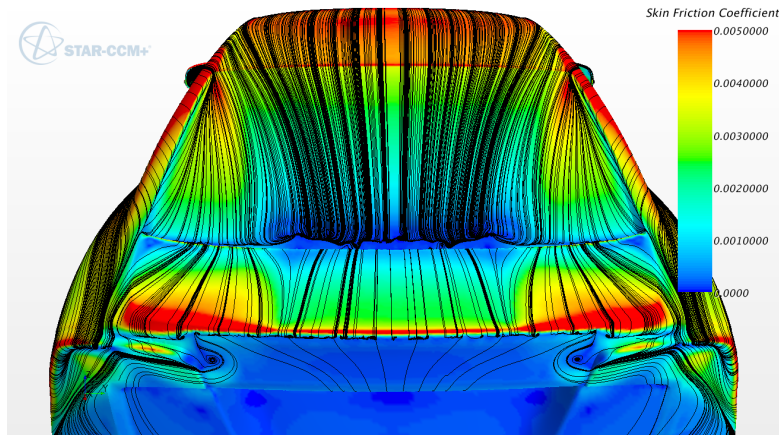


Figure 4.9: Skin friction coefficient with streamlines at 100 kph.

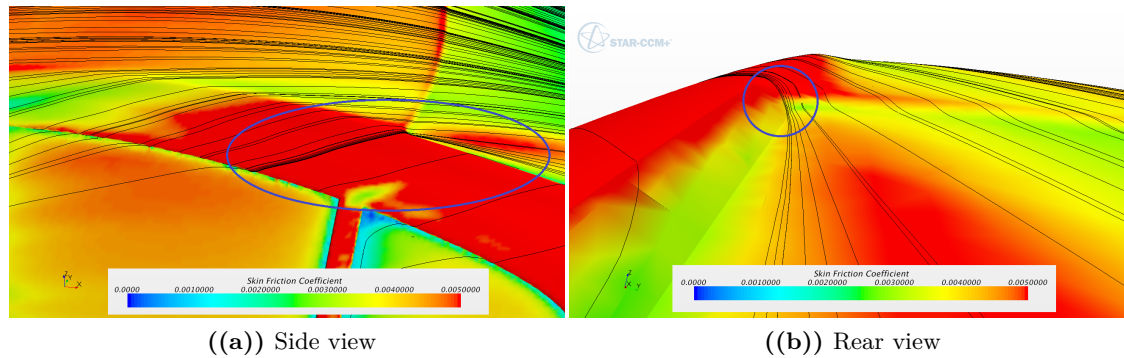


Figure 4.10: Diverging streamlines, accelerating over the C-pillar, at 100 kph.

A-pillar. As the vortex passes this area, it influences the flow coming from the C-pillar by pushing it towards the window, as seen in Figure 4.11. The rotation of the vortex is illustrated by the vorticity in the x-direction, as seen in Figure 4.12. Positive vorticity equals anti-clockwise rotation, and negative vorticity equals clockwise direction. An easy way of thinking about it is to compare it with the right-hand rule used in mathematics and physics with the thumb pointing in the flow direction. Hence, this means that the left vortex is pushing the flow down and contributes to the high skin friction area.

The high skin friction area over the roof indicates an attached flow. This assertion is even more strengthened by Figure 4.6 showing the high velocity on the roof and thus there is no separation occurring.

Following the flow to the rear, the flow close to the surface starts to slow down. This can be seen in 4.13 and is due to the change in geometry from the rear window to the boot lid. A flow close to the surface with low speed often runs a higher risk of separation. At

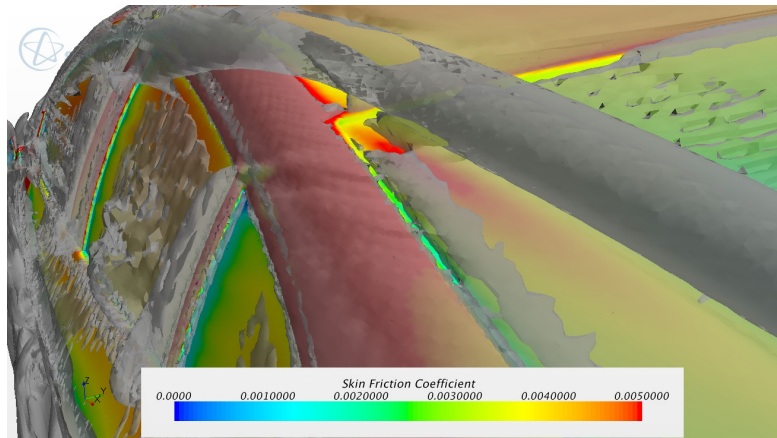


Figure 4.11: Q-criterion with isovalue 100 visualized on a skin friction plot at 100 kph.

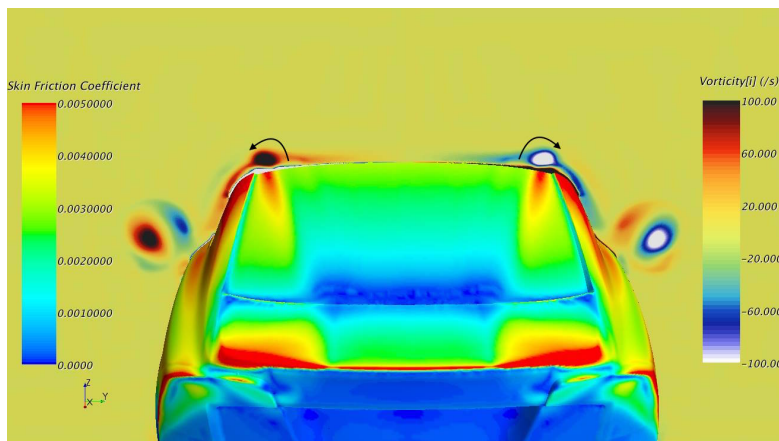


Figure 4.12: Vorticity in an yz-plane with skin friction coefficient at 100 kph.

this area there is partial separation occurring as can be seen by the low velocity close to the surface in Figure 4.14. This plays a key role in explaining the next high skin friction area at the trailing edge of the boot lid since this flow reattaches at the trailing edge, which creates a high skin friction area there.

Figure 4.13 shows a continuous flow pattern with an abrupt change over the trailing edge where the speed is higher. This strengthens the assumption that there is an attached flow since speeds close to zero mean the flow is separated and higher speeds are an indication of an attached flow.

Low skin friction coefficient

Areas characterised by low skin friction are areas where the flow runs a higher risk of separation. The rear of the car shows two large areas with low skin friction which can

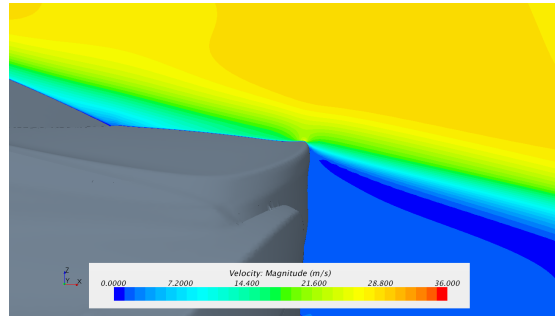


Figure 4.13: Symmetry plane with velocity at 100 kph.

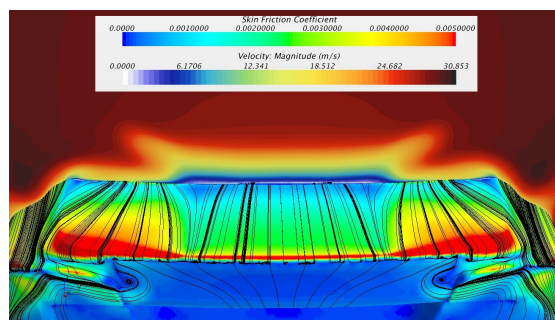


Figure 4.14: Crossplane with velocity and skin friction at 100 kph.

be seen in Figure 4.9. The first area, at the centre of the window and boot lid, and the second area, at the rear of car.

As shown in Figure 4.13 and Figure 4.14 the flow is partially separated in the middle area of the rear window. A visualization with streamlines, Figure 4.15, shows a uniform flow over the rear window until it reaches the bottom where swirls occur. These swirls could be the result of the edge of the boot lid which slows and stops the flow. These swirls combined with the partially separated flow are likely to be the cause for the low skin friction area.

The second low skin friction area is at the vertical area of the boot lid and has a straight forward explanation. As can be seen in Figure 4.6, the area behind the vertical area of the boot lid is characterized by a low velocity area. This is what is creating the low skin friction, and is due to the separation from the boot lid. The separation most likely occurs due to the sudden change in geometry from an almost horizontal plane on the boot lid to a vertical plane.

Reynolds dependency of the skin friction coefficient

When studying the skin friction coefficient with varying speeds there is one distinguishable pattern as seen in Figure 4.16, the areas characterized by high skin friction get

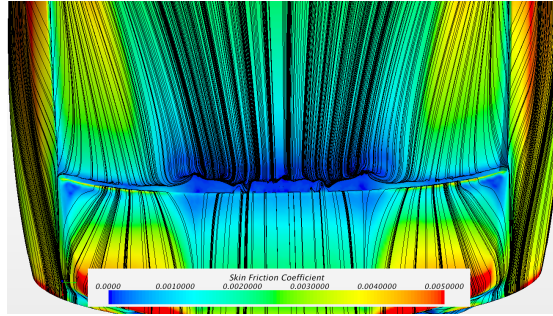


Figure 4.15: Skin friction coefficient with streamlines over the rear window and boot lid at 100 kph.

smaller. Note that this does not mean that the shear stress on the high skin friction areas gets lower with higher velocity, but that the ratio between the shear stress and velocity does. This phenomenon, that the skin friction coefficient generally is lower with higher Reynolds number, has been tested and proved numerous times [22]. For all velocities investigated the skin friction coefficient scenes are presented in Appendix C.

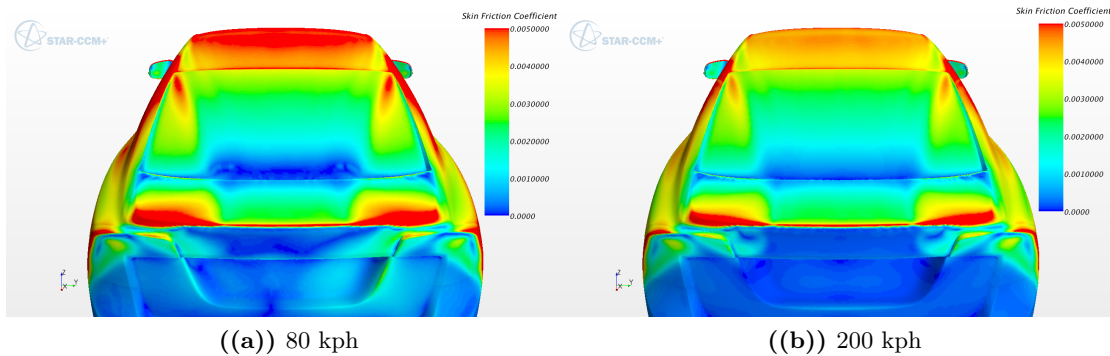


Figure 4.16: The effects of a higher velocity on the skin friction coefficient.

Another noticeable difference is that between the 80 kph case and the 100 kph the change in the skin friction coefficient is larger than between any other velocity changes. This could have two reasons. Firstly, the skin friction coefficient declines somewhat exponentially with higher Reynolds number and thus the drop is bigger between 80 and 100 kph than between 120 and 140 kph [22]. Secondly, the mesh was refined at this area by altering the prism layer settings; more about this in section 3.2.2.

Finally, there is one area, the lower part of the rear window, that is characterized by a slightly lower skin friction coefficient in the 80 and 100 kph case than the other velocities. An explanation of why this low skin friction area forms is presented above in the section low skin friction. In this area the skin friction coefficient actually increases and thus

contradicts what has been stated earlier. The reason for this could be that with higher velocity, the swirls are pushed downwards and thus also the area with low skin friction is pushed downwards. Other than that, a comparison of the skin friction shows a quite similar distribution.

4.4 Antenna Study

This section will present the results for the simulations performed with the antenna in order to analyze the impact on the flow structure. The velocity is kept constant at 100 kph for both the antenna and the non-antenna case.

4.4.1 Drag coefficient

Table 4.2 provides the drag coefficient values and the change in frontal area for the two different cases. The drag coefficient only varies on the drag count, which indicates that the antenna has low effects on the overall drag coefficient. However, it is important to understand that the flow structure can still be altered and other phenomena acting on the car may behave differently. This will be further discussed in the remaining part of this section.

Table 4.2: Drag coefficient and frontal area.

Type	C_D	Frontal area increase [m^2]
Without antenna	0.256	-
With antenna	0.257	3.87E-4

4.4.2 Surface pressure coefficient

By studying the pressure coefficient over the rear window for the antenna case, interesting observations can be made. The comparison with and without antenna in Figure 4.17 shows that a more concentrated high pressure coefficient area is formed at the transition from the rear window to the boot lid for the case with antenna.

The velocity is affected by the antenna which is shown in comparison with the no antenna case in Figure 4.18. This shows a higher velocity closer to the surface, suggesting an attached flow. Though, at the window to boot lid transition, the velocity rapidly decreases which is not the case without the antenna. Thus, a more focused area of high pressure is created.

By including the antenna in the simulation a new obstacle on the roof is created. This means that the flow that occurred in the case without the antenna gets disrupted. This can be visualized by looking at the Q-criterion, Figure 4.19. Here the flow is disrupted

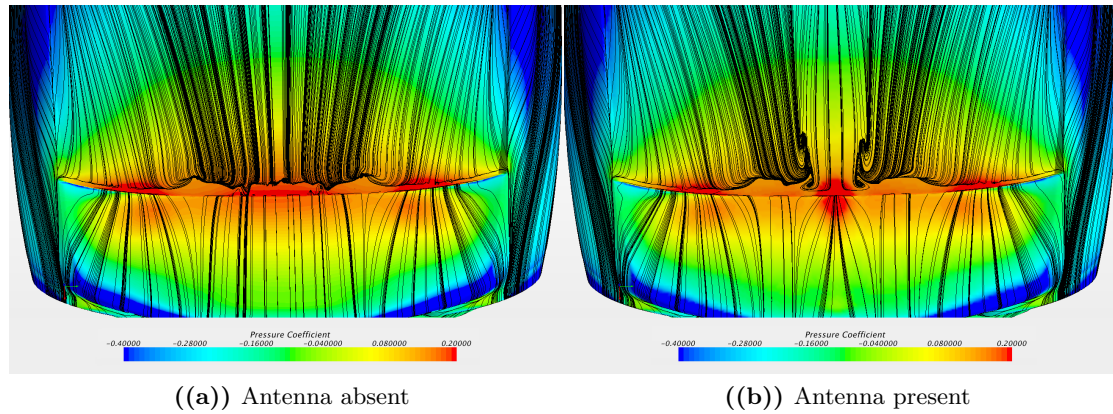


Figure 4.17: The effects of the antenna on the pressure coefficient with limiting streamlines.

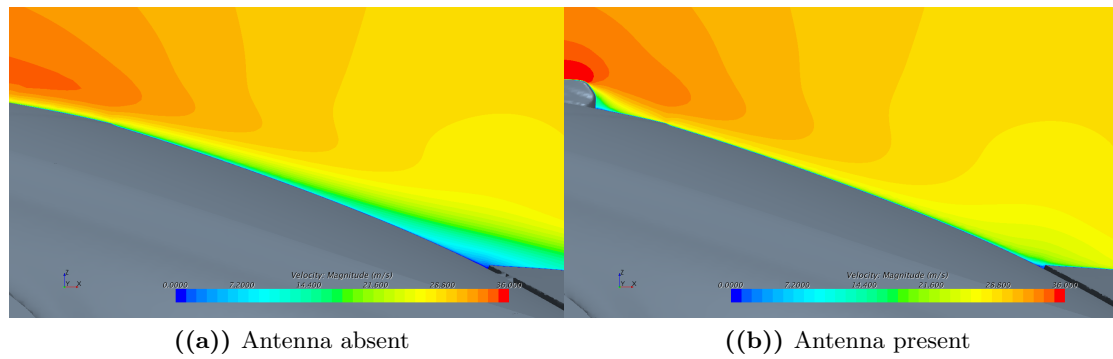


Figure 4.18: Velocity profile on the symmetry plane.

and two vortices are created, forming due to crossflow separation, which occurs at the antenna. A more thorough explanation of this can be found in section 2.1.5. Worth noting is that these vortices flow above the rear window and not on the surface of the car. These vortices decrease in intensity when moving further down over the rear window, but pick up again at the transition from the rear window to the boot lid, as seen in Figure 4.19(b).

Although some of the intensity is lost, the vortices are still present. When the air flowing over the window comes to a halt at the window/boot lid transition, an upward motion of the flow is created. As the flow loses velocity at this transition, the concentrated high pressure area in the centre of the window, shown in Figure 4.17(b), is created. The flow then connects to the already introduced vortices created at the antenna.

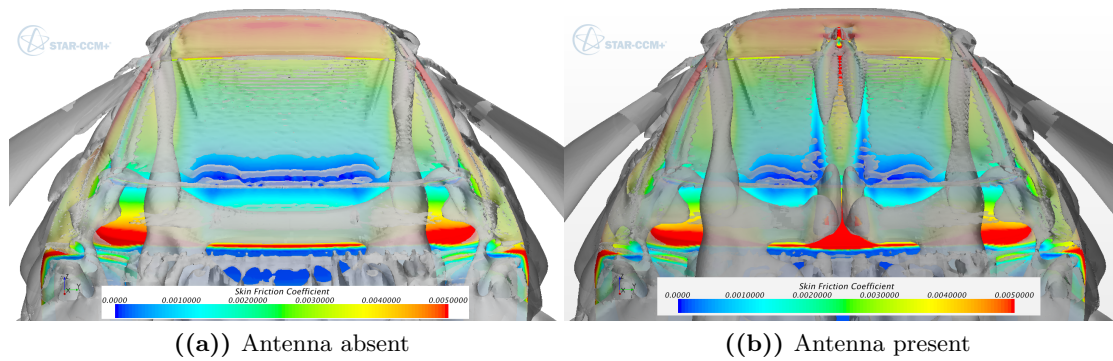


Figure 4.19: Effects of the antenna on the Q-Criterion at isovalue 300.

When the flow separates from the boot lid, a wake behind the car is created. As explained in section 2.1.7, wakes are characterized by recirculating flow causing lower velocity in the region. Figure 4.20 shows the velocity profile on a symmetry plane, with an indication line of where the bulk flow starts to differ from the wake flow. In this figure, the wake seems to be smaller with the antenna present. However, the indication lines are drawn at almost the same places. This may indicate that the flow is only affected around the centre line. By illustrating the total pressure coefficient as an isosurface, Figure 4.21 shows that the wake structure is identical, except for the inward bend in the centre.

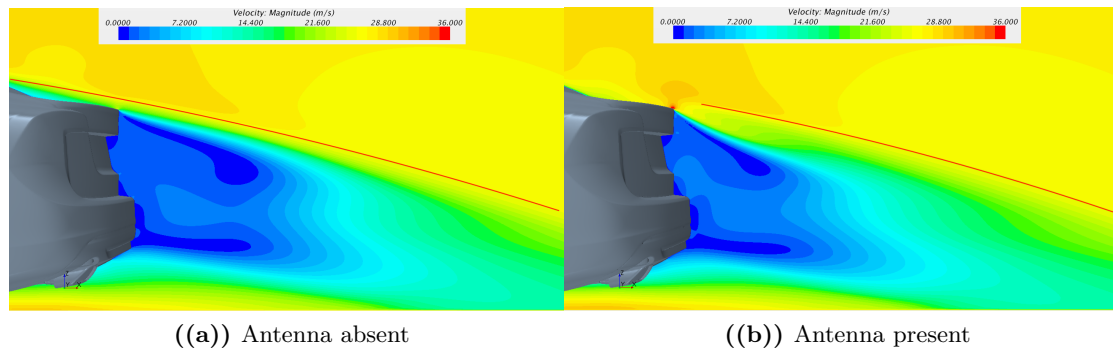


Figure 4.20: Wake behind the car with an indication line that marks the boundary between the bulk flow and the wake flow.

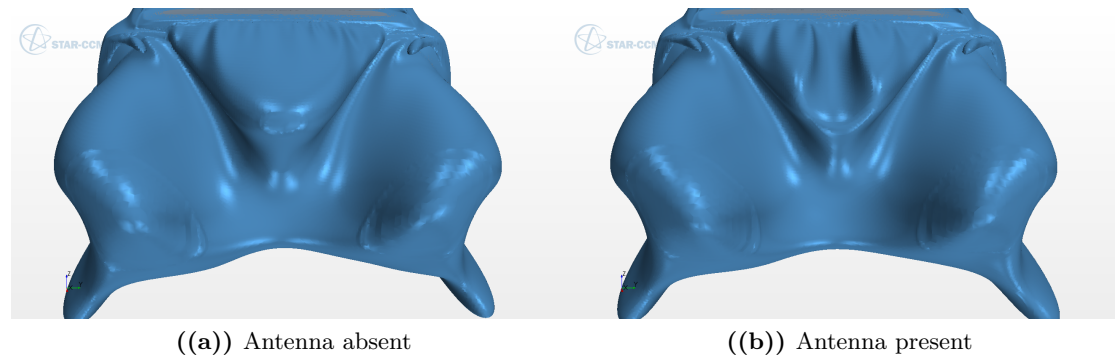


Figure 4.21: Total pressure coefficient on an isosurface with isovalue 0.

4.4.3 Skin friction coefficient

In section 4.3.3, an explanation of the creation of high and low skin friction coefficient areas was given. Now, with the antenna taken into consideration, the structure of the skin friction coefficient diverges from the case without the antenna. This is shown in Figure 4.22 by the skin friction coefficient with constrained streamlines on the surface. The structural alteration is obvious with the creation of a new high skin friction coeffi-

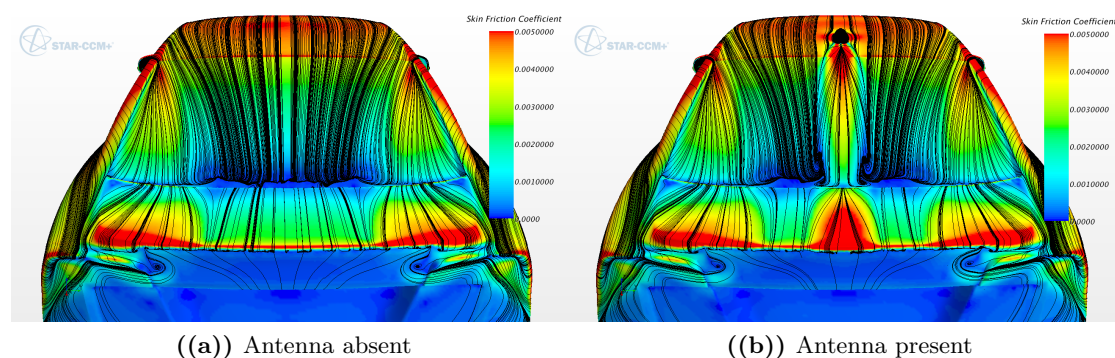


Figure 4.22: Effects of the presence of an antenna on the skin friction pattern.

cient behind the antenna and at the boot lid. This also correlates with the streamlines that coincide behind the antenna and at the window/boot lid transition. The coincided streamlines then distribute over the high skin friction area. The fact that the streamlines are gathered in the beginning of these areas suggests that the flow is attached.

The low skin friction coefficient area at the rear window has been divided into two sections. These observations indicate that the separation locations have shifted and that the vorticity structures now could be different. To confirm this, a scene illustrating the Q-criterion was set up and is shown in Figure 4.23. As these figures show, the vorticity pattern is different with the antenna. The high skin friction coefficient behind the

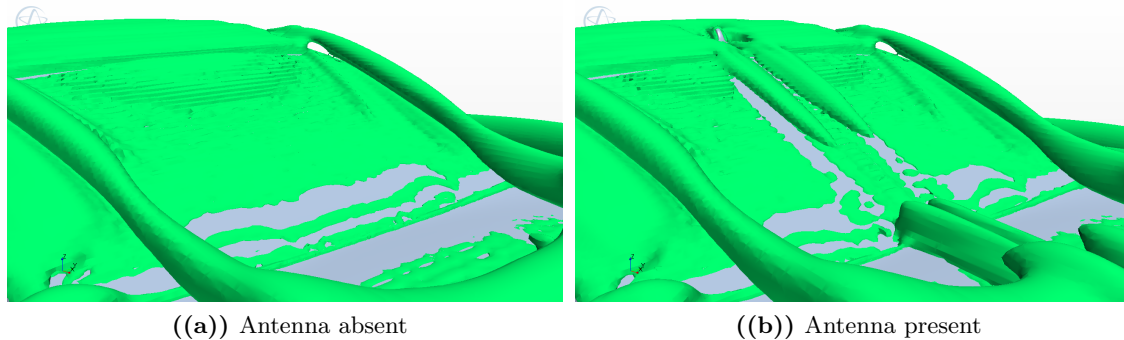


Figure 4.23: Effects of the presence of an antenna on the Q-Criterion at iso value 100.

antenna is due to a flow that merges over the antenna and converges behind it. This is further discussed in [3],[8].

Two vortices are created from the antenna, one on each side, and can be traced all the way to the end of the boot lid. The high skin friction coefficient together with no extensive volume shown by the Q-Criterion, indicates that the flow is somewhat attached from the antenna to the boot lid. Figure 4.19(b) shows that the vortices coming from the antenna, are detached from the surface and the flow under them is attached. By illustrating the vorticity in the x-direction on a crossplane behind the antenna, as in Figure 4.24, it could be shown that both vortices are rotating towards the antenna when looking from above. This contributes to the high skin friction behind the antenna, caused by air being pressed down, allowing the flow to stay attached. Although the skin

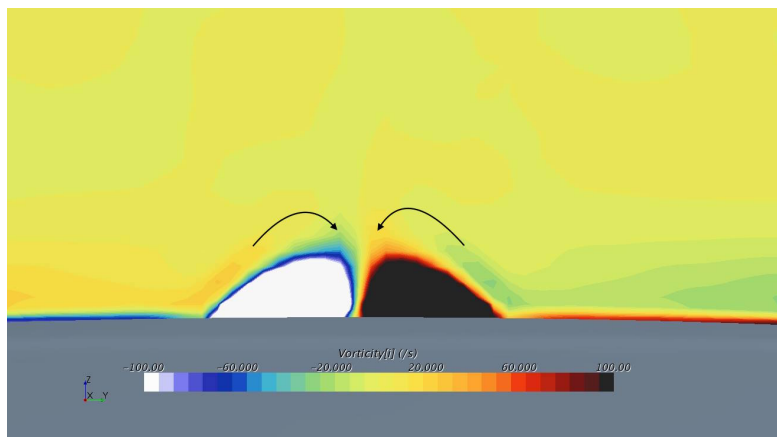


Figure 4.24: Vorticity on a crossplane 5 cm behind the antenna, showing the direction of rotation.

friction is lower at the rear window to boot lid transition, this does not mean that the flow has to be separated as explained in section 2.1.5.

Figure 4.6 showed that the velocity is higher over the roof, meaning that the flow has accelerated and is attached. When the flow travels past the antenna similar effects take place, as shown in Figure 4.25. Figure 4.25(a) shows an increased velocity over the antenna and Figure 4.25(b) shows that the velocity is higher over the antenna than its surroundings.

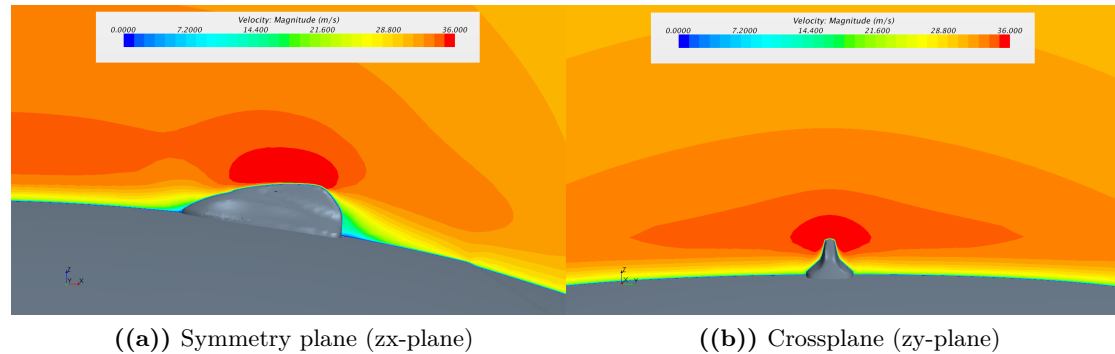


Figure 4.25: Crossplanes showing how the antenna affects the velocity.

By studying Figure 4.22(b), the streamlines show a recirculation at the bottom of the window. As the flow moves over the roof it converges at the bottom of the window, moving towards the centre. At the centre, the flow from the side encounters the attached flow which acts almost like a wall, stopping the flow from traveling further. This is creating something that looks like bubble separation, with two different flows that can not enter each others regions.

This can also be illustrated by the velocity profile with a crossplane at the transition, seen in Figure 4.26(a). In the centre bottom, the crossplane shows a relatively high velocity which indicates an attached flow. On both sides of the described area, the velocity is lower which indicates a separated flow.

Following the flow to the end of the boot lid, the centre line flow is still attached as seen by the high skin friction coefficient. The velocity crossplane can also be used here to detect the presence of vortices. Figure 4.26(b) shows that the velocity is lower over the area of lower skin friction coefficient. At the higher skin friction coefficient areas, the velocity is also higher which indicates an attached flow. This can also be seen in Figure 4.23(b), where the Q-Criterion does not show the presence of vorticity at the high skin friction coefficient areas.

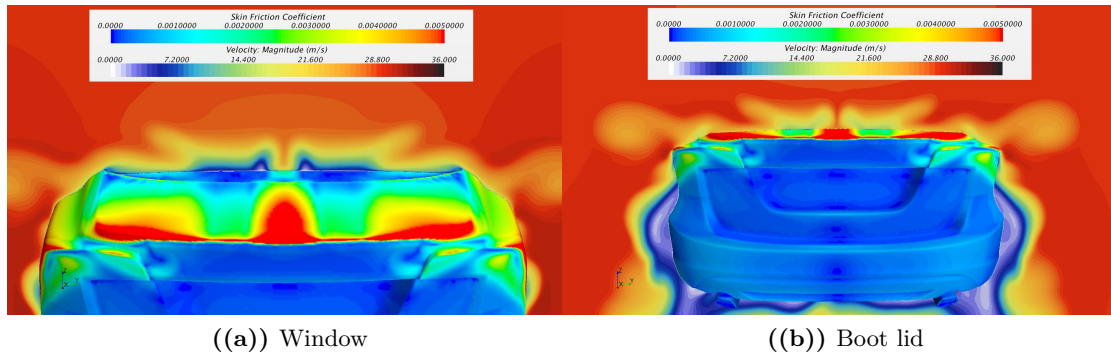


Figure 4.26: Crossplanes showing how the antenna affects the velocity.

4.5 Yaw Angle Dependency

In this section, the results for the yaw angle dependency will be presented, analyzed and explained. As stated previously, there were four yaw angles used: 0° , 2.5° , 5° and 10° . The aim of this section is to investigate whether there is any relation between an increasing yaw angle and certain physical properties.

4.5.1 Drag coefficient

A varying yaw angle will affect the flow structure on the car and thus create a change in drag coefficient. This suggests that the drag coefficient value increases or decreases with an increase in yaw angle, and will not stay constant as opposed to the Reynolds sweep [23]. In table 4.3 the drag coefficient values for varying yaw angles of the Volvo S60 are presented.

Table 4.3: Drag coefficient for varying yaw angles.

Yaw angle [$^\circ$]	C_D
0	0.257
2.5	0.263
5	0.282
10	0.297

As can be seen by studying the drag coefficient values for increasing yaw angles the drag coefficient increases. This means that this study, just like previous ones, supports the claim that the drag coefficient is dependent on the yaw angle [23]. To give an easier overview of the drag coefficient's dependency it is also displayed in a graph below, Figure 4.27.

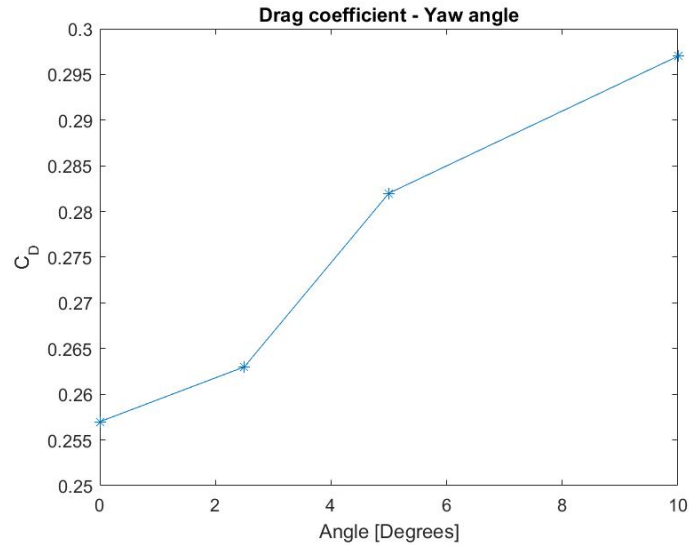


Figure 4.27: Graph of drag coefficient vs. yaw angle.

4.5.2 Surface pressure coefficient

In the 0° yaw case, the high pressure coefficient areas are concentrated to three areas mainly on the rear window, as seen in Figure 4.8. As the yaw angle increases, these areas become spread out towards the right.

The high pressure coefficient area emerging from the antenna, explained in 4.4.2, broadens and moves slightly. But other than that, it does not change much. However, the two other high pressure coefficient areas change more. Already at 2.5° yaw the change is noticeable, as can be seen in Figure 4.28(b). The left high pressure coefficient area broadens and another area characterized by a high pressure coefficient is created on the boot lid. These two areas continue growing for every increase in yaw angle. This might not be totally unexpected. Since as the yaw angle increases, there is a shift in the flow and thus, the air hitting the rear window and boot lid flows from the B-pillar and C-pillar instead of over the roof, see Figure 4.28. This also moves the swirls created by the antenna, which are incapable of affecting the flow as before. Therefore more flow is halted at the boundary between the rear window and boot lid creating a high pressure coefficient area.

For the high pressure coefficient area to the right there is just a minor alteration. As can be seen in Figure 4.28, the area to the right gets smaller and starts to move immediately with an increase in yaw angle. The reason for this could be that with an increase in yaw angle, the flow shifts and instead of flowing from over the roof, the flow travels from both the roof and the side of the car. Thus, the high pressure coefficient area moves. This is visualized by the limited streamlines over the car in Figure 4.29.

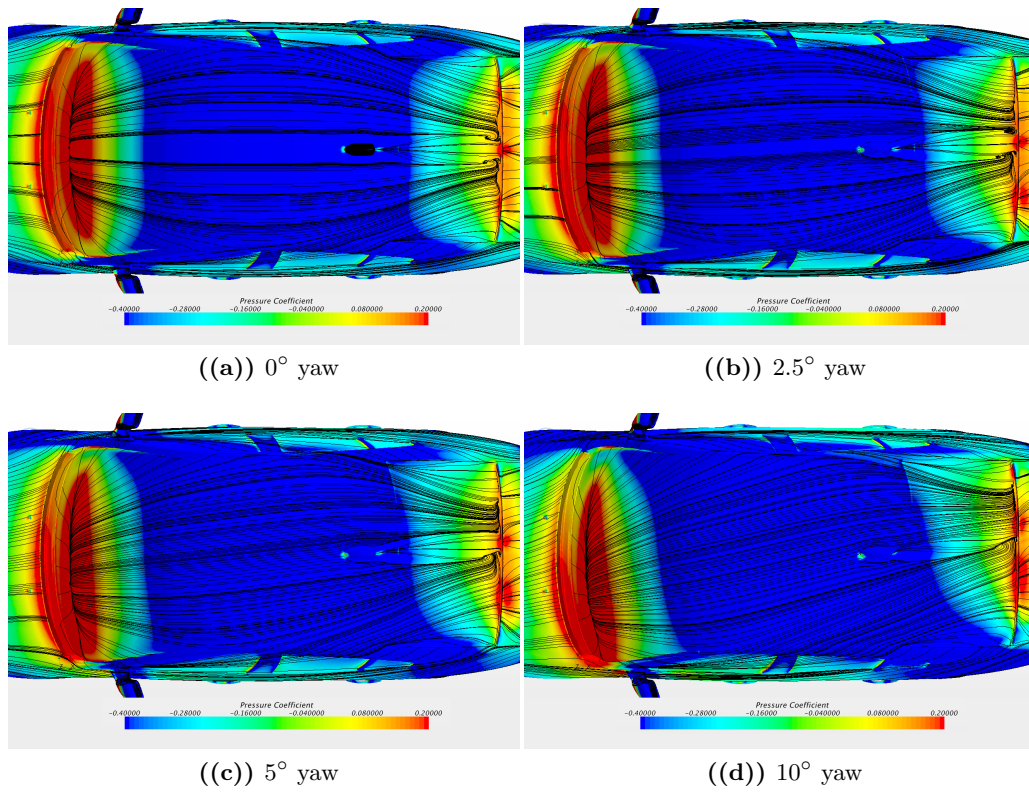


Figure 4.28: Pressure coefficient for a varying yaw angle.

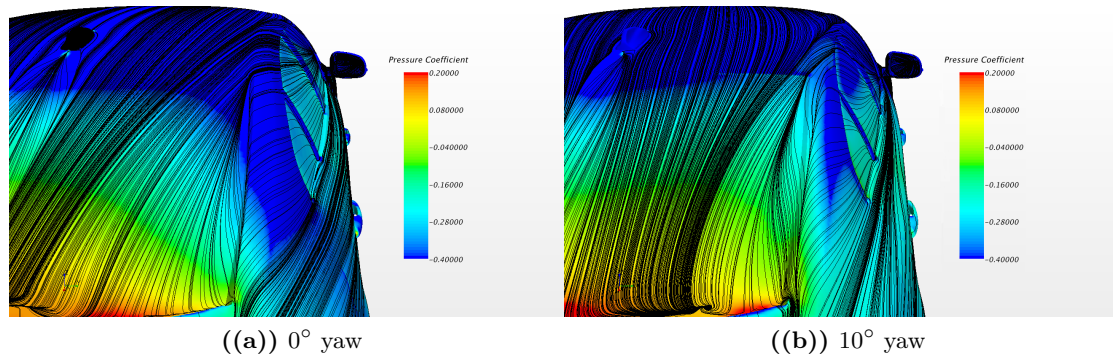


Figure 4.29: Pressure coefficient for 0° and 10° yaw with streamlines.

Finally, an overall observation is that as the yaw angle increases the pressure coefficient distribution gets skewed to the right.

4.5.3 Skin friction coefficient

By comparing the four cases in Figure 4.30, for increasing yaw angles it can be seen that the skin friction areas are shifted increasingly towards the right side. This is likely due to the fact that by increasing the yaw angle, the air flows more from the left.

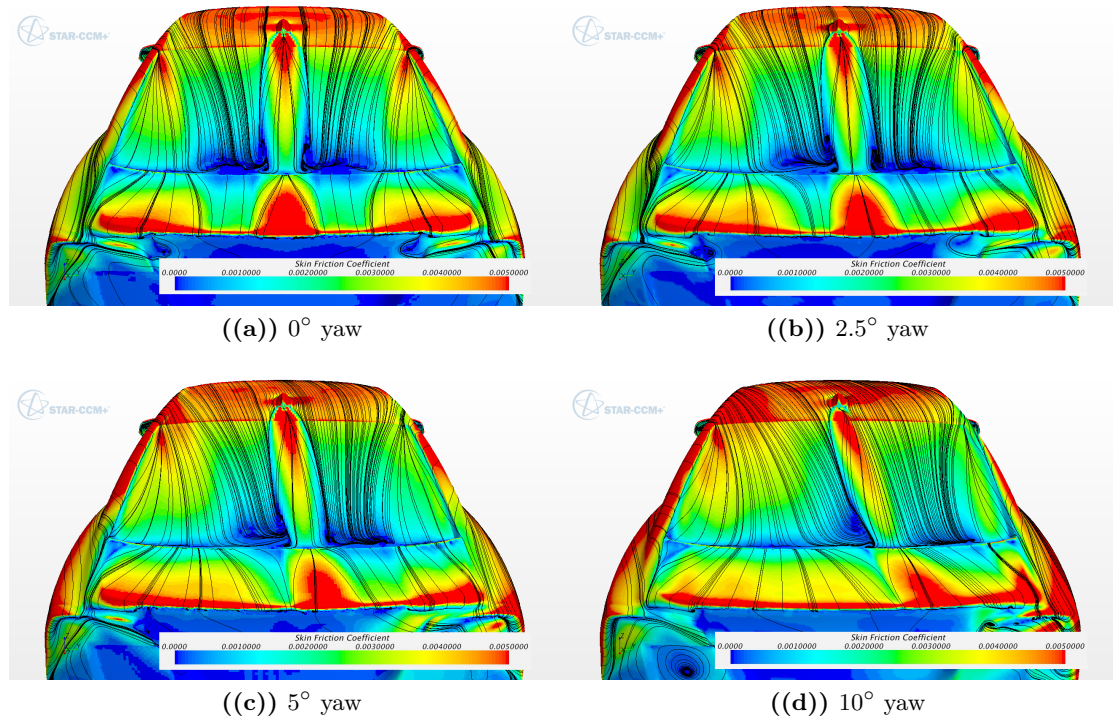


Figure 4.30: Skin friction for a varying yaw angle.

Figure 4.30 clearly shows that the high skin friction coefficient area at the top right corner of the rear window disappears with an increase in yaw angle. This is due to two changes. Firstly, the lack of flow, which in 0° yaw, accelerates over the transition from the C-pillar to the rear window, as explained in section 4.3.3. Secondly, the new path of the vortex which forms from the A-pillar. At 0° yaw, as seen in Figure 4.19(b), this vortex affects and pushes the flow against the window creating more skin friction, as explained in section 4.3.3. But with yaw, for instance 10° yaw as seen in Figure 4.31, this vortex flows over the side of the car and does not affect the flow over the rear window.

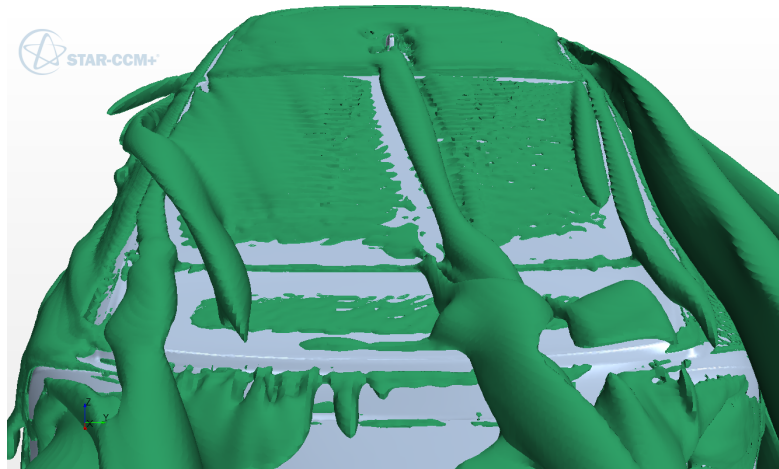
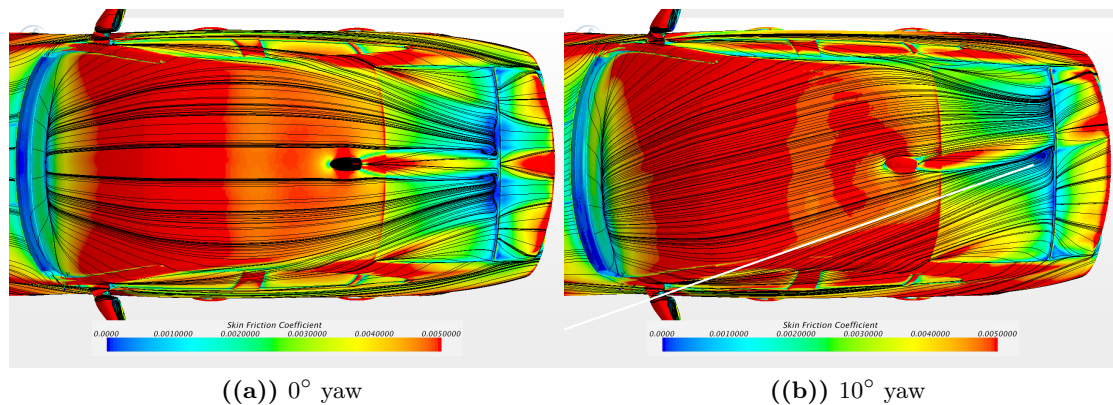


Figure 4.31: Q-criterion at 10° yaw with isovalue 300.

Additionally, it can be seen that the area on the rear window that arises from the antenna impeding the flow is also present in the yaw angle cases. However, the area too is shifted. The reason for this could be that the antenna still experiences a similar flow at 10° yaw, as at 0° yaw, but from another angle. This assertion is strengthened by studying the streamlines over the roof of the car, Figure 4.32. The white line marks the boundary between the flow traveling from the windscreen and the flow traveling from over the side of the car. Clearly, the flow affecting the antenna at 10° yaw, flows from over the windscreen and over the roof just as in the 0° yaw case, and thus the high skin friction area acts the same.



((a)) 0° yaw

((b)) 10° yaw

Figure 4.32: Skin friction with streamlines.

5

Discussion

In this chapter a discussion of the obtained results will be presented. Specifically, the discussion will delve into the reasons why these results were obtained. This will be done by studying not just one parameter, but rather all parameters presented in the last chapter.

5.1 Reynolds Dependency

The results presented are purely from simulations and a lot of effects taking place on the road are not taken into consideration. The whole study is focusing on the effects on these coefficients from the actual car body, which hopefully will help in understanding the effects on the flow from the body of the car. There are a few physical restraints that affect the results such as closed engine bay and using steady-state on the flow in the simulation. This makes the actual numbers non-realistic but since all numbers were calculated in the same conditions they are comparable.

To be able to discuss this with regards to the Reynolds number, it is first essential to understand what is happening. One area with an interesting flow structure is the area on the bottom part of the rear window. This area is characterized by three high pressure coefficient zones and an area with low skin friction as explained in sections 4.3.2 and 4.3.3 and seen in Figures 4.8 and 4.9. The sides of the widely spread low skin friction area, reach slightly higher than the rest of the area. At these places, the pressure coefficient is also lower as a result of the high pressure coefficient zones. With the limited streamlines applied, an interesting observation can be made; the streamlines diverge from the high pressure areas and move to the sides and slightly upwards on the low skin friction area creating foci. The reason for this flow structure could be that less flow is traveling over these areas. Thus, nothing pushes the flow down. At the area where the streamlines form into foci, separation in the form of horn separation most

likely occurs. The theories about separation and the observation that the streamlines do not push as far down as in the high pressure zone, are even more strengthened by the low skin friction areas since this is an indication of separation. This means that if the flow is not attached, it will not be able to push further down either.

By studying this area with regards to the Reynolds number another interesting observation can be made. An increase in Reynolds number leads to a slight increase in pressure coefficient and a slight increase in the skin friction coefficient. The increase in skin friction would suggest that the flow stays attached longer. This is supported by the limited streamlines which at 200 kph have been forced all the way down to the boot lid. Once more, the same trend at a lower velocity is shown; the streamlines diverge from the high skin friction areas and create foci. The reason for the movement of the streamlines, higher pressure and higher skin friction could be that with higher velocity, more air gets stuck in the gap between the rear window and boot lid. This means that a higher pressure will form, and a higher skin friction due to an attached flow further down the window.

On the vertical part of the boot lid there is a low pressure area because of the wake. When the car moves it creates a region behind it, which is characterized by a recirculating low velocity fluid. When there is movement in a flow the skin friction coefficient usually changes with the velocity, however in this particular area there is low velocity movement and no attached flow and therefore no skin friction either.

The discussion indicates that an increase in Reynolds number leads to variation in the pressure coefficient and the skin friction coefficient. It also affects the origin of the foci by being pushed further down over the rear window. However, this does not affect the drag coefficient, which only fluctuates with one drag count.

5.2 Antenna Impact

The antenna causes a clear alteration of the flow structure behind the car, which is shown in Figures 4.17, 4.22 and 4.23. The centre point at the bottom of the rear window is an interesting area when studying all the different parameters. This area is experiencing higher pressure, skin friction and velocity than its surroundings. This is not the case without the antenna, when there is a more uniform distribution over the rear window. The explanation for this is traced to the flow phenomena occurring at the antenna, and will have to be explained first. When the flow reaches the antenna, two vortices are created due to crossflow separation. But this does not apply for all the flow over the antenna. Due to a favourable design of the antenna, it was shown in Figure 4.24 that the vortices are rotating in such way that they are pressing the surrounding flow towards the surface. This contributes to the high skin friction area behind the antenna, located under and between the vortices. In a sense, this acts like a tripwire with the abruptness of the flow, but not in a sense that it trips the flow from laminar to turbulent, since all

flow in this case is turbulent.

With the phenomena occurring at the antenna explained, the interpretation of the area at the centre bottom of the rear window is easier to comprehend. The high skin friction behind the antenna indicates an attached flow between the two vortices from the antenna. Figure 4.18 shows a higher velocity closer to the surface, thus indicating an attached flow, but with an abrupt decrease at the bottom window. Higher surface pressure can be detected by a lower velocity, but to confirm this, the limiting streamlines are helpful. Figure 4.23(b) shows recirculating streamlines on the sides of the high pressure area. The studied and presented figures involving pressure and limited streamlines show that the streamlines are being pushed away from high pressure areas. It is now presumable that the flow over the centreline of the rear window is attached and experiences a lower velocity when reaching the boot lid. This may cause the surrounding flow to be pushed to the sides, making a swirling motion. Together with the flow coming from the sides of the rear window, the flow from several foci causing horn separation.

In the centre, at the beginning of the boot lid, a nodal point can be detected. The flow that separates at the bottom of the window now attaches and stays attached until the end of the boot lid. On the sides of the centre high skin friction area, there are areas of lower skin friction. Together with the lower velocity over these areas, illustrated in a crossplane in Figure 4.26(b), this suggests a partially separated flow.

Due to the notchback design, the bulk flow hits the end of the boot lid. Thus, the high skin friction line along the boot lid edge is created. This could have been avoided with a fastback design, allowing the flow to follow the surface without the encounter of a collision.

In this discussion several alterations of the flow structures were shown. However, when the results of the drag coefficient are presented, the increase of drag coefficient is only one drag count. Since cars are bluff bodies, the drag is dominated by pressure drag. The alteration to the wake created behind the car is fairly small. This suggests that the skin friction increase over the rear window has little effect on the total drag. Although the flow structure alteration is considerable, this explains why the antenna is kept in the newer Volvo S60 designs.

5.3 Yaw Angle

Changing the yaw angle causes obvious changes to the flow structure, by shifting the flow towards the right side for an increasing yaw angle. However, the flow structures still show the same pattern as for 0° yaw with almost the same high skin friction and high pressure coefficient areas present.

The rear window is a good example of how the varying yaw angle shifts the flow struc-

tures. The vortices present at the rear of the car also change. The vortices that arise from the A-pillars and flow over the roof and rear window change drastically for 10° yaw. The left vortex disappears while the right side vortex flows at the side of the car which is shown in Figure 4.31. This is understandable since the flow hits the left A-pillar from an angle which divides the flow to the side and over the front window. Therefore it does not flow over the A-pillar edge which causes separation. This is however present at the right side with the flow over the front window which separates at the right A-pillar edge and a vortex emerges which flows past the right side. There is also a vortex present at the left side of the rear window which originates from the base of the side mirror. This vortex trails along the side of the car and turns over the C-pillar, as seen in 4.31. All vortices present are greatly affected by the yaw angle.

Observing the pressure coefficient distribution for 10° yaw it is skewed over the rear window compared with the 0° yaw distribution which is seen in Figure 4.28. Studying the streamlines over the rear window, it can be shown that the flow enters at the top right corner, where the pressure coefficient was increased, from the roof for 10° yaw compared with from the C-pillar for 0° yaw. This is shown in Figure 4.30. The flow from the side of the car enters the roof and flows to the top corner of the rear window where the streamlines then diverge downwards, as seen in Figure 4.29. Additionally, the skin friction decreases in the same corner for an increasing yaw angle. However, there is still some skin friction left, as seen in Figure 4.30. As the skin friction increases downwards and the streamlines diverge it indicates an attached flow at the top corner of the rear window. The high skin friction zone present there for 0° yaw disappears for 10° yaw. This might be due to the flow entering the rear window over a smoother edge, roof to rear window, compared with the C-pillar edge. Also the right side A-pillar vortex which pushed the flow downwards is not present anymore.

On top of the C-pillar there is an increase in pressure coefficient, decrease in skin friction and converging streamlines which suggest separation occurs there. This is shown in Figure 4.29. Two interesting vortices emerge on top of the C-pillar and the right side of the rear window.

The left side of the rear window also yields some interesting observations. At the top left corner of the rear window the pressure coefficient decreases as more streamlines diverge away from this area. This is seen in Figure 4.28. Additionally, the skin friction in the same area increases, seen in Figure 4.30. The decrease in pressure, increase in skin friction and the diverging streamlines suggest that the flow on the left side of the rear window is attached. Why the skin friction zone is still present at the left side compared with the right side, even though both sides lost their A-pillar vortex, might be due to that the flow is still attaching there and accelerating over the C-pillar.

6

Conclusion

In this chapter the conclusions on whether the pressure coefficient, drag coefficient and skin friction coefficient are dependent on the velocity and yaw-angle will be presented. Additionally, the impact of the antenna is presented as well. It also contains suggestions and tips for anyone who chooses to do further study in the same area. This section ends with an evaluation of the study and the methods and errors that have arisen.

6.1 Reynolds Dependency

The pressure coefficient showed slight variations when changing the velocity. The three pressure areas on the transition from the back window to the boot lid kept the same form on all the velocities but increased in the area they covered. This showed that the pressure coefficient was Reynolds dependent.

After analyzing the results it could be shown that the skin friction was dependent on the velocity. With higher velocity, the high skin friction coefficient areas, got lower. The overall conclusion was that the skin friction coefficient was Reynolds dependent.

There were slight changes in the drag coefficient values, but the differences were small. While the skin friction coefficient and pressure coefficient showed some changes, the drag coefficient only changed with one drag count. Thus, the drag coefficient did not show a Reynolds dependency. One of the more important aspects of this study was to see whether the drag coefficient was Reynolds dependent or not. While the skin friction coefficient and pressure coefficient were Reynolds dependent it did not affect the drag coefficient in any significant way.

6.2 Antenna Impact

The antenna is an object, placed in the middle of the flow over the roof which suggests that it is going to affect the upcoming flow structure. However, the presence of an antenna did not affect the drag coefficient to a high degree, only differing by one drag count.

There were interesting changes in flow structure and the distribution of the pressure coefficient between the antenna and the non antenna case. The antenna case showcased a higher pressure coefficient at the transition from the rear window to the boot lid. There were also certain similarities between the antenna case and the non antenna case in terms of pressure coefficient: with the exception of the aforementioned zone (the transition from rear window to boot lid), the pressure coefficient is similarly distributed on the boot lid and the rear window for both cases.

Finally, the skin friction coefficient also exhibited certain changes in flow structure and distribution when an antenna was present. A higher skin friction area on a thin strip of the rear window and the boot lid, behind the antenna, was observed. However, it should be noted that both cases displayed similar skin friction distributions on the sides of the window and the boot lid.

The antenna study can be summarized as showing that the pressure coefficient and the skin friction coefficient are affected rather dramatically by the presence of an antenna. However, it showed that the drag coefficient was not highly affected by the antenna. The areas that showed the most alteration were the transition between the boot lid and the rear window, and the narrow area on the rear window and boot lid. The sides on both the rear window and the boot lid showed similarities between the antenna case and the non antenna case.

6.3 Yaw Angle

The pressure coefficient is characterized by three areas, mainly over the rear. With an increase in yaw angle these areas move in the same direction as the shift of the flow. Another observation was that the high pressure coefficient areas over the rear, broadened with an increase in yaw angle. This indicates that the pressure coefficient is dependent on the yaw angle.

The same pattern could be found for the skin friction coefficient. An increase in yaw angle led to a shift in the flow over the car. This meant that the skin friction coefficient distribution shifted, and thus it is also yaw angle dependent.

Lastly, the drag coefficient also changed with variations in yaw angle. For the four cases investigated, the drag coefficient increased.

The overall conclusion is thus that the flow structures occurring on the car, seem to be yaw angle dependent. This leaves the drag coefficient to increase with an increase in yaw angle for the investigated cases.

6.4 Further Study

There were many areas that were not taken into consideration in this project due to time constraints. As such, there is considerable room for further investigation.

This project was mainly focused on the rear of the car; many other parts such as the underbody and the wheels would yield many interesting results in terms of flow structures. Another aspect that could be further studied would be the use of a finer mesh; a finer mesh could provide a more accurate solution and would aid the analysis. Additionally, a larger variety of velocities and yaw angles could be used to aid in establishing patterns for analysis. A further possibility for future work is investigating the effect of fluid mechanics models on flow structures. This could be done by experimenting with different fluid mechanics models in the simulation environment. This would provide data for analysis and would also highlight the differences in accuracy between various models.

Finally, it would be beneficial to perform the same scenario in a physical wind tunnel as opposed to solely relying on software simulations. Additional results from a physical wind tunnel test would serve as a suitable comparison with the computer simulation.

6.5 Evaluation

The method was solely computer simulations where the wind tunnel scenario was recreated in a virtual environment. The results were then compared with aerodynamics theory to see if they were plausible. Since no full size wind tunnel experiment had been made it caused uncertainty where the theory failed to apply. Some wind tunnel results were provided by the supervisor, S.Bonitz, but only some were comparable to the achieved results.

In the numerical solving the turbulent model $k-\varepsilon$ was used and compared with other models available, and was found to be coarse. Other models might get a more accurate solution but require a finer mesh and more processing time which is a common trade-off that has to be made; more accurate results against time spent. Another factor was the number of prism layers used, which affects the resolution of the boundary layers. Having more prism layers goes hand in hand with a finer turbulent model.

The simulations done were executed with steady-state conditions, which is an approximation of the reality in one time frame. Thus, simplifications were made when solving, since time-dependent results are neglected. As aerodynamics in reality is not steady-state, this is a big factor on the deviation of the result.

The simulations of the environment made, fulfil open road conditions better than the wind tunnel which the results were compared with. In the simulations all of the ground was moving, compared to only a conveyor belt for the wheels, and the size of the simulated wind tunnel is not as limited as the real one was. Having a too narrow wind tunnel affects the surrounding flow.

Bibliography

- [1] M. White. *Fluid Mechanics*. New York: McGraw Hill Higher Education, 7th edition, 2011.
- [2] G. T. Chapman and L. A. Yates, "*Topology of Flow Separation on Three-Dimensional Bodies.*" *Applied Mechanics Reviews*, vol. 44, no. 7, p. 329, 1991.
- [3] Bonitz S., Löfdahl L., Larsson L. and Broniewicz A., "*Investigation of three-dimensional flow separation patterns and surface pressure gradients on a notchback vehicle.*" In international vehicle aerodynamics conference, [S.l.], Woodhead, 2014, pp. 55-65.
- [4] S.Kida, "Life, Structure, and Dynamical Role of Vortical Motion in Turbulence", <http://www.igf.fuw.edu.pl/IUTAM/ABSTRACTS/Kida.pdf>, [2016-03-07, 11:00]
- [5] Sims-Williams, D., Marwood, D., and Sprot, A., "*Links between Notchback Geometry, Aerodynamic Drag, Flow Asymmetry and Unsteady Wake Structure,*" *SAE Int. J. Passeng. Cars – Mech. Syst.* 4(1):156-165, 2011, doi:10.4271/2011-01-0166.
- [6] Nouzawa, T., Haruna, S., Hiasa, K., Nakamura, T. et al., "*Analysis of Wake Pattern for Reducing Aerodynamic Drag of Notchback Model*", SAE Technical Paper 900318, 1990, doi:10.4271/900318.
- [7] Jenkins, L., "*An Experimental Investigation of the Flow Over the Rear End of a Notchback Automobile Configuration*", SAE Technical Paper 2000-01-0489, 2000, doi:10.4271/2000-01-0489
- [8] Bonitz, S., Larsson, L., Lofdahl, L., and Broniewicz, A., "*Structures of Flow Separation on a Passenger Car*", *SAE Int. J. Passeng. Cars - Mech. Syst.* 8(1):177-185, 2015, doi:10.4271/2015-01-1529
- [9] Wieser, D., Lang, H., Nayeri, C., and Paschereit, C., "*Manipulation of the Aerodynamic Behavior of the DrivAer Model with Fluidic Oscillators*", *SAE Int. J. Passeng. Cars - Mech. Syst.* 8(2):687-702, 2015, doi:10.4271/2015-01-1540

- [10] <http://www.cd-adapco.com/>, Basic overview of CFD, z100EU [Online tutorial] 2016-03-31, 11:25
- [11] L. Davidson, "An Introduction to Turbulence Models" Department of Thermo and Fluid Dynamics. CHALMERS UNIVERSITY OF TECHNOLOGY. Göteborg, Sweden, January 14, 2015
- [12] <http://www.ne.se/uppslagsverk/encyklopedi/l%C3%A5g/lamin%C3%A4rt-ytskikt>, Nationalencyklopedin, [2016-04-13, 13:40]
- [13] <http://www.ne.se/uppslagsverk/encyklopedi/l%C3%A5g/turbulens/>, Nationalencyklopedin, [2016-04-13, 14:10]
- [14] Gajendra Singh, M., Nagpurwala, Q. H., Abdul Nassar and Shankapal, S. R. "Numerical Investigations on Crosswind Aerodynamics and its Effect on the Stability of a Passenger Car", SAE Paper No. 2009-26-059
- [15] P. Theissen, J. Wojciak, K. Heuler and R. Demuth, T. Indinger and N. Adams "Experimental Investigation of Unsteady Vehicle Aerodynamics under Time-Dependent Flow Conditions - Part 1", 2011-01-0177 Published 04/12/2011
- [16] <http://stevedocs.cd-adapco.com>, Steve-portal [Online manual] 2016-04-13, 11:42
- [17] <https://www.sharcnet.ca/Software/Fluent6/html/ug/node480.htm>, Sharcnet 2016-04-13, 11:00
- [18] <http://stevedocs.cd-adapco.com>, Steve-portal [Online manual] 2016-04-13, 11:17
- [19] L. Chen, <http://www.math.uci.edu/~chenlong/226/FVM.pdf>, Finite Volume Methods, 2016-04-12, 11:00
- [20] H.K Versteeg and W.Malalasekera. *An Introduction to Computational Fluid Dynamics: The Finite Volume Method*. Longman Scientific Technical, Harlow, UK, 1995.
- [21] Finite Difference, Finite Element and Finite Volume Methods for Partial Differential Equations, Joaquim Peiro and Spencer Sherwin, Department of Aeronautics, Imperial College, London, UK
- [22] Joseph, C., Klewicki, "Reynolds Number Dependence, Scaling, and Dynamics of Turbulent Boundary Layers", ASME Technical Paper 2010-09-23, 2010, doi:10.1115/1.4002167
- [23] Wieser, D., Schmidt, H., Müller, S., Strangfeld, C. et al., "Experimental Comparison of the Aerodynamic Behavior of Fastback and Notchback DrivAer Models" SAE Int. J. Passeng. Cars - Mech. Syst. 7(2):682-691, 2014, doi:10.4271/2014-01-0613. '

- [24] Stephen K. Norfleet, Wall Effects Evaluation
,<http://www.rmb-consulting.com/newspaper/wall/wall.htm>, RMB Consulting
Research, Inc., 2016-05-14, 11:00

Appendix A

y^+ Values

Figures showing the range of Y^+ values for different cases.

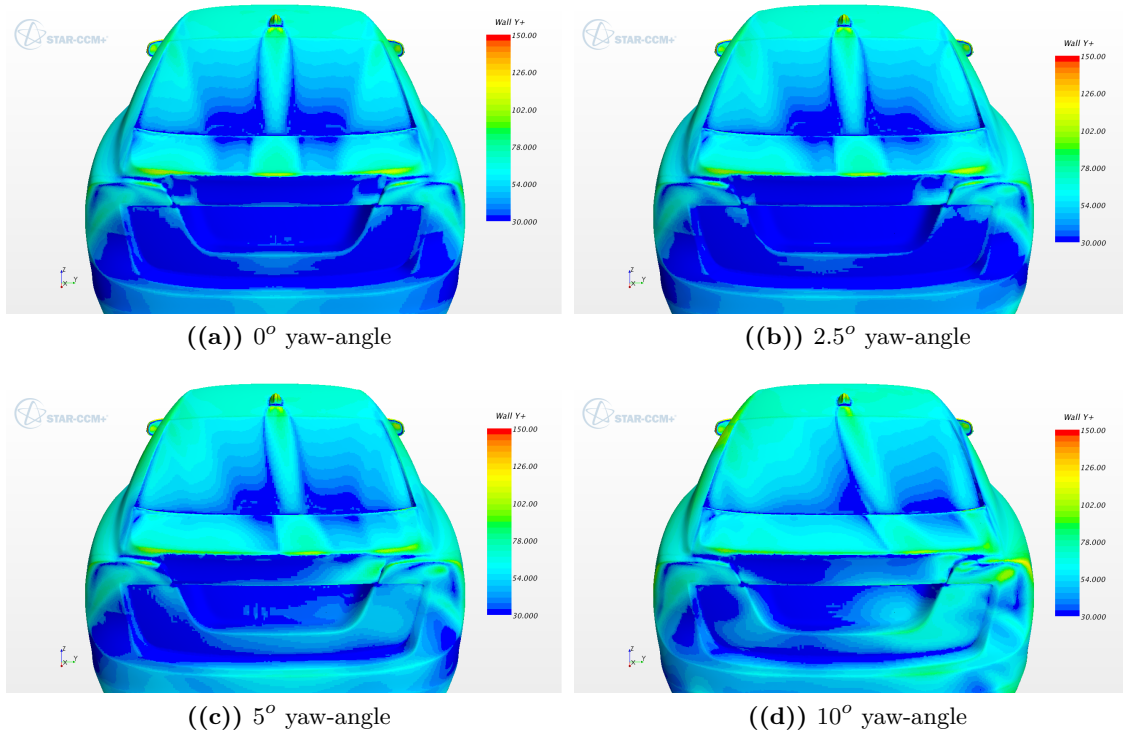


Figure A.1: Y^+ values for $0^\circ, 2.5^\circ, 5^\circ$ and 10° yaw-angle.

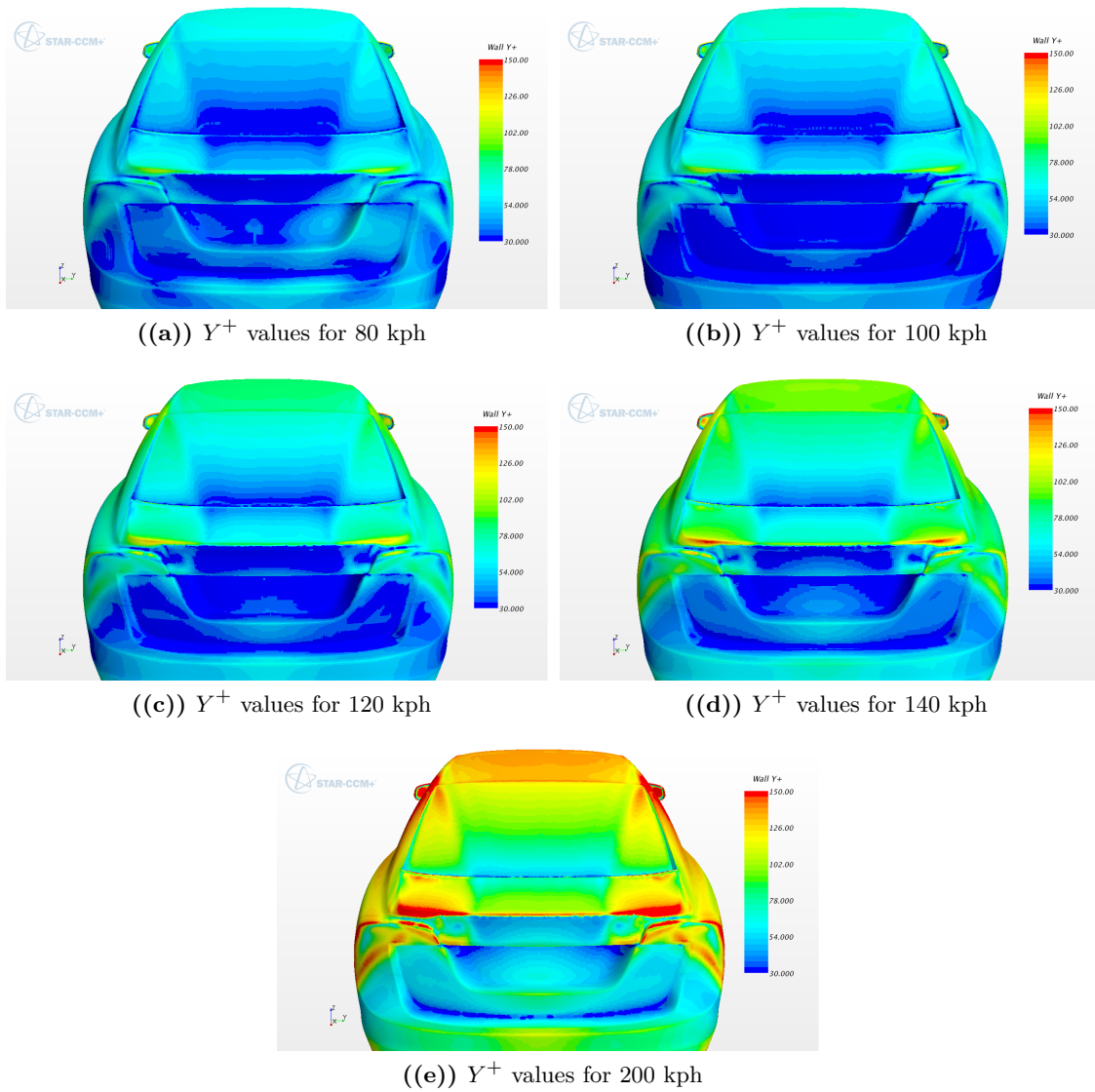


Figure A.2: Y^+ values for 80, 100, 120, 140 and 200 kph cases.

Appendix B

Surface Pressure Coefficient

Figures showing the C_p coefficient at different velocities. Notice the graduate change at the bottom end of the back window.

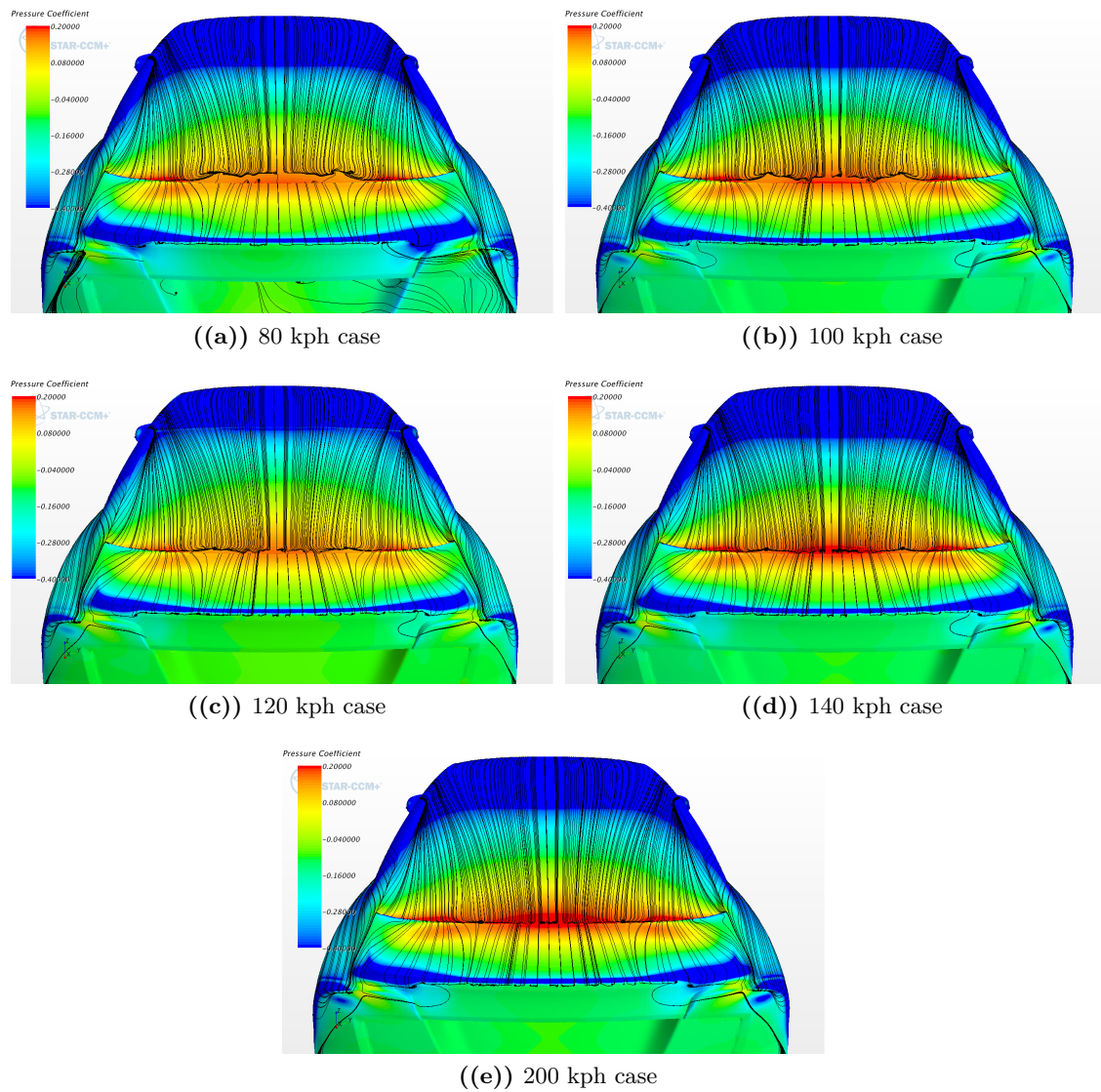


Figure B.1: Surface pressure coefficient on the rear of the car in 80, 100, 120, 140 and 200 kph case.

Appendix C

Skin friction coefficient

Figures showing the C_f coefficient at different velocities. Notice how in some areas the C_f decreases the fast the flow moves.

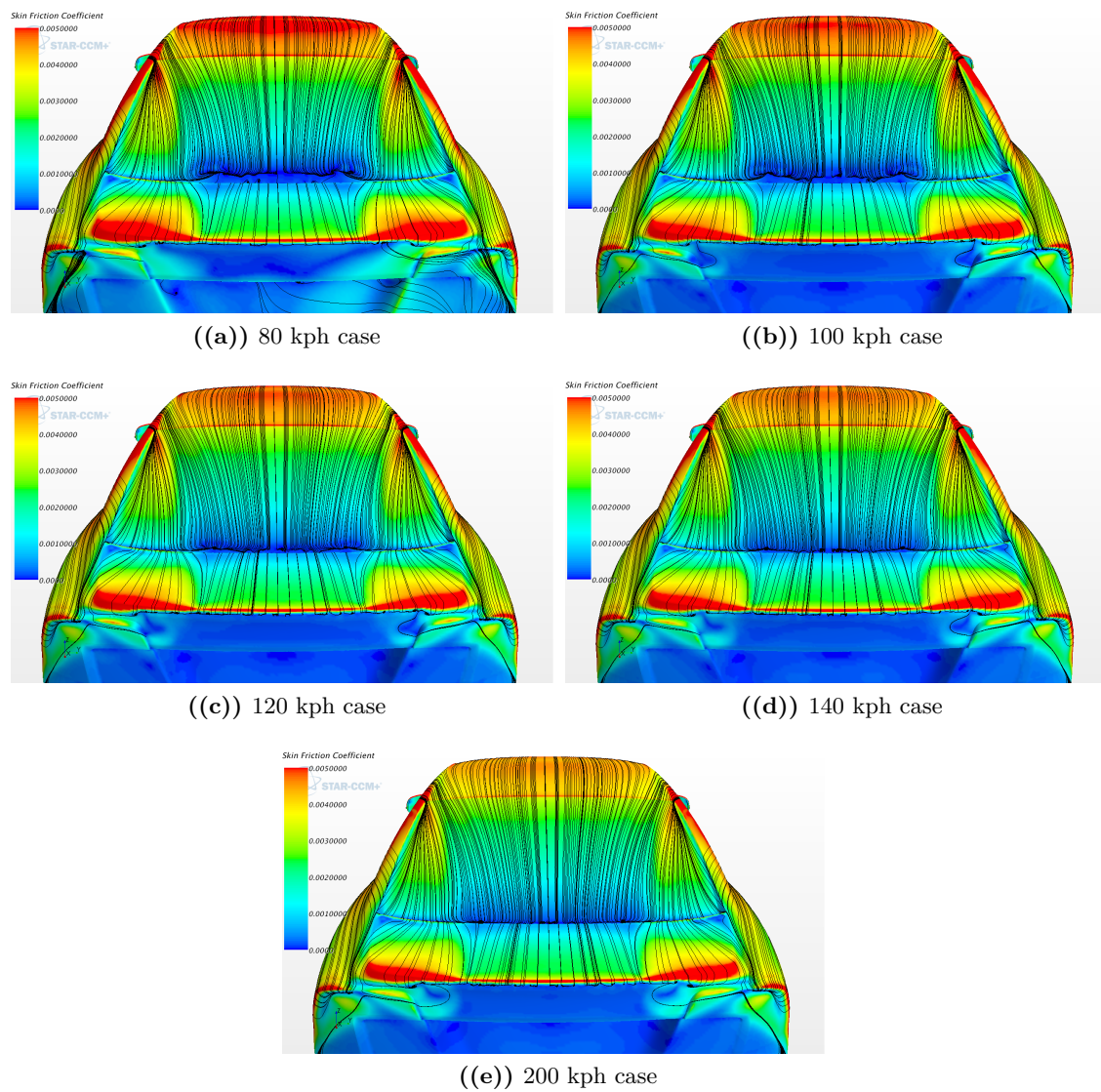


Figure C.1: Skin friction coefficient on the rear of the car in 80, 100, 120, 140 and 200 kph case.